ACADEMIC PRESS

Available online at www.sciencedirect.com

SCIENCE DIRECT®

Journal of Sound and Vibration 262 (2003) 245–289

JOURNAL OF SOUND AND VIBRATION

www.elsevier.com/locate/jsvi

Transient vibration phenomena in deep mine hoisting cables. Part 2: Numerical simulation of the dynamic response

S. Kaczmarczyk[a,*,1], W. Ostachowicz[b]

[a] *School of Mechanical Engineering, University of Natal, Durban 4041, South Africa*

[b] *Institute of Fluid Flow Machinery, Polish Academy of Sciences, 14 Fiszera Street, 80-952, Gdansk, Poland*

Received 30 May 2001; accepted 2 May 2002

Abstract

A simulation model is presented which investigates the dynamic response of a deep mine hoisting cable system during a winding cycle. The response, namely the lateral motions of the catenary cable and the longitudinal motion of the vertical rope with conveyance is observed on the fast time scale, and the slow time scale is introduced to monitor the variation of slowly varying parameters of the system. The cable equivalent proportional damping parameters, and periodic excitation functions resulting from the cross-over cable motion on the winder drum are identified. Subsequently, the model is solved numerically using parameters of a double-drum multi-rope system. Since the system eigenvalues are widely spread and the problem is of stiff nature, the numerical simulation is conducted using a stiff solver. The results of the simulation demonstrate various transient non-linear resonance phenomena arising in the system during the wind. The nominal ascending cycle simulation results reveal adverse dynamic behaviour of the catenary largely due to the autoparametric interactions between the in- and out-of-plane modes. Principal parametric resonances of the lateral modes also occur, and conditions for autoparametric interactions between the lateral and longitudinal modes arise. Additionally, a transition through a number of primary longitudinal resonances takes place during the wind. The adverse dynamic motions in the system promote large oscillations in the cable tension which must be considered significant with respect to fatigue of the cable. It is noted that a small change in the winding velocity may cause large changes in the dynamic response due to the resonance region shifts. Consequently, the resonance modal interactions can be avoided, to a large extent, if the winding velocity is increased to an appropriate level.

*Corresponding author. Tel.: +44-1604-893158; fax: +44-1604-792650.

E-mail address: stefan.kaczmarczyk@northampton.ac.uk (S. Kaczmarczyk).

[1] Presently at the School of Technology & Design, University College Northampton, St. George's Avenue, Northampton NN2 6JD, UK.

0022-460X/02/$ - see front matter
doi:10.1016/S0022-460X(02)01148-3

1. Introduction

The use of computer-aided dynamic simulation has become an effective tool for the analysis and design of mechanical systems in many fields. These include transport, and systems such as automobiles, trucks, trains, lifts, aircraft, and many others. The components used in these applications are subjected to large displacements, and their geometric configuration undergoes large variations under normal operating conditions. Also, travelling distance ranges, loads and speeds are continuously being increased, and consequently, higher accelerations and inertial forces are being generated in structural members. Thus, it is of great importance that the dynamic response of the system be predicted in detail during all design stages. This is particularly true in the case of vertical transport systems employed in the mining industry. For example, in the South African gold mining industry new mines with shaft depths in the region of 3000–5000 m, based on single-lift winding, have recently been considered [1]. Consequently, parameters like the winding cycle acceleration/deceleration, winding speeds, winder hoisting capacities, and many other have to be carefully considered at any design stage.

A typical mine single-lift winding installation comprises a driving winding drum, a steel wire cable, a sheave mounted in headgear, and a conveyance. In this system, the cable forms a horizontal or inclined catenary between the drum and the sheave, and a vertical rope hangs below the headsheave. Thus, this configuration is referred to as the catenary–vertical rope system. It is known that the dynamic behaviour of this system may demonstrate complex vibration phenomena that include non-linear modal interactions between lateral oscillations of the catenary cable and longitudinal oscillations of the vertical rope [2]. Therefore, an efficient formulation of a mathematical model describing the dynamic response, and an application of stable numerical algorithms are the pivot elements in achieving successful response simulation results. The mathematical model of the catenary–vertical rope system has been formulated by Kaczmarczyk and Ostachowicz in a companion paper Part 1 [3]. This model is given in the form of a non-linear slowly varying ordinary differential equation system with external and parametric excitation terms, with quadratic couplings between the lateral and the longitudinal modes, and a cubic coupling between the in- and out-of-plane lateral modes. The natural frequencies of the system vary slowly during the winding cycles, and a passage through a number of resonances occur.

Some of the resonance locations can be shifted when the winding velocity is changed. Thus, a suitable winding strategy can be designed to avoid an excessive dynamic response. In this paper, the results of numerical simulation of equations of motion are presented to confirm this strategy. It is taken into account that the natural modes of the system are widely spaced during the wind and that the problem is of a *stiff* nature. Consequently, a stiff integration algorithm is employed to simulate the dynamic behaviour of the system.

2. Simulation model

2.1. Equations of motion

The equations of motion of the system have been derived using Hamilton's principle and the Rayleigh–Ritz procedure, with the lateral and longitudinal motions expanded in terms of the

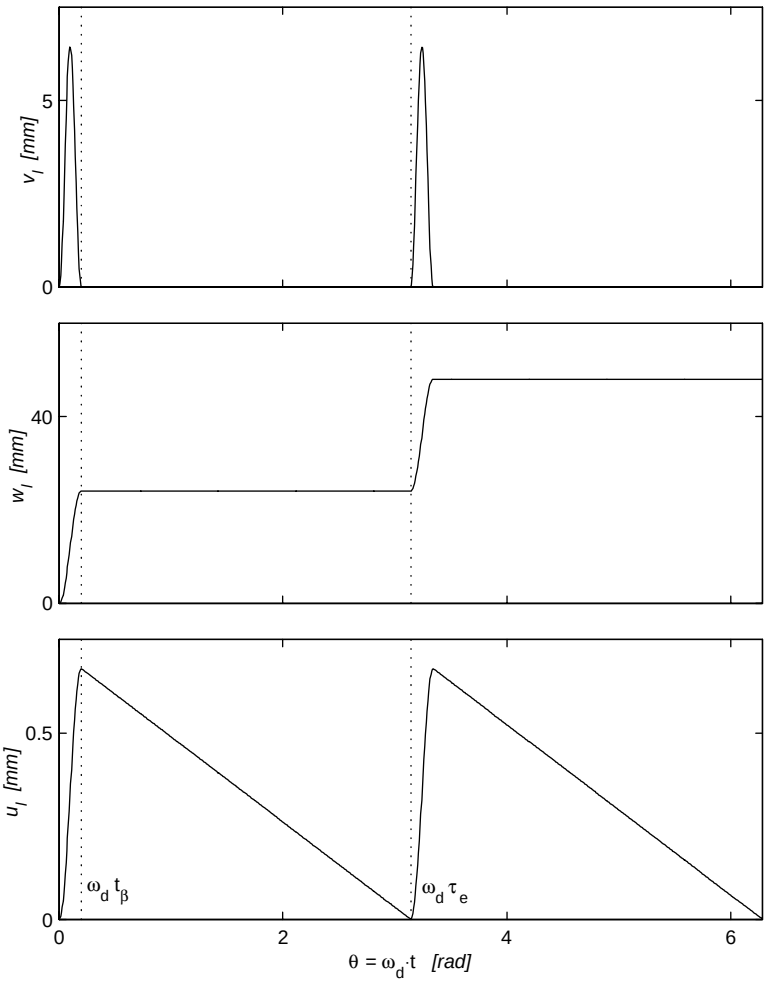

Fig. 1. Plots of the cross-over excitation functions versus angle of rotation of the winder drum $\theta \in [0, 2\pi]$ rad for a typical set of parameter values: $d = 0.048$ m, $R_d = 2.14$ m, $V_c = 15$ m/s, and $\beta = 0.2$ rad.

corresponding linear free-oscillation modes. The details are given in Part 1, and consequently, the nomenclature used in this study is consistent with that used in the companion paper (a list of symbols is given in the nomenclature). It should be noted that in this formulation two time scales are used to monitor the system dynamic behaviour. The lateral and longitudinal oscillations are observed on the fast time scale defined as $T = \omega_0 t$, where ω_0 is the initial fundamental frequency of the entire system. Since the system parameters, namely the natural frequencies and the equation coefficients, vary slowly, the slow time scale $\tau = \varepsilon T$, where ε is a small, positive, dimensionless parameter, is also introduced. Consequently, in this analysis the system is represented in the matrix form as

$$\dot{\mathbf{y}} = \mathbf{A}(T, \tau; \varepsilon)\mathbf{y} + \mathbf{N}(\tau, \mathbf{y}) + \mathbf{F}(T, \tau), \tag{1}$$

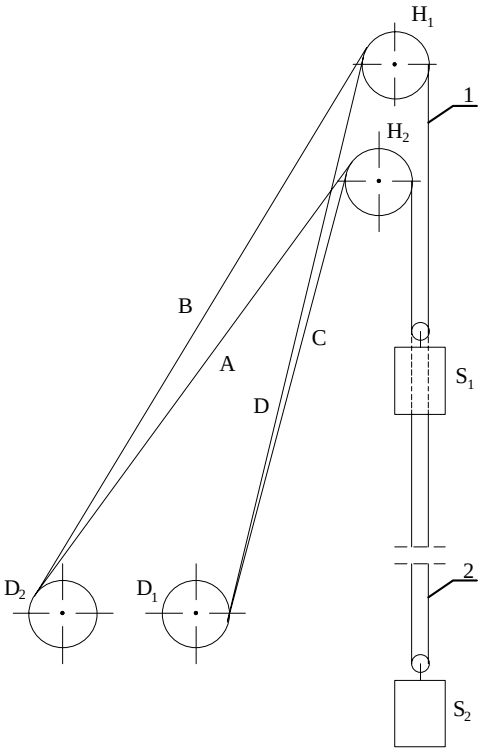

Fig. 2. A double-drum Blair multi-rope (BMR) system.

Table 1
Parameters of BMR winder

Maximum hoisting velocity (m/s)	15
Weight of skip and bridle (kN)	180
Load on skip (kN)	165 ± 10
Winder drum diameter (m)	4.27
Sheave wheel diameter (m)	4.27
Cable diameter (m)	48×10^{-3}
Cable linear density (kg/m)	8.49
Cable type	6-strand Lang's play
Number of layers on winder drum	4
Length of catenaries A, B, C, D (m)	74.4, 79.6, 69.8, 75.3
Maximum depth of wind (m)	2085

where $\mathbf{y} = [\mathbf{p}^{\mathrm{T}}, \mathbf{q}^{\mathrm{T}}, \mathbf{z}^{\mathrm{T}}, \dot{\mathbf{p}}^{\mathrm{T}}, \dot{\mathbf{q}}^{\mathrm{T}}, \dot{\mathbf{z}}^{\mathrm{T}}]^{\mathrm{T}}$ is the 2 $(2N_{lat} + N_{long})$-dimensional modal state vector, with $\mathbf{p} = [p_1, p_2, ..., p_{N_{lat}}]^{\mathrm{T}}$, $\mathbf{q} = [q_1, q_2, ..., q_{N_{lat}}]^{\mathrm{T}}$ and $\mathbf{z} = [z_1, z_2, ..., z_{N_{long}}]^{\mathrm{T}}$, where N_{lat} and N_{long} represent the numbers of the lateral and longitudinal modes, respectively, and dots denote differentiation

Table 2
Kloof simulation parameters

Number of lateral modes N_{lat}	4
Number of longitudinal modes N_{long}	4
Total winding cycle time (s)	156
Acceleration/deceleration time (s)	19.7
Nominal hoisting velocity V_c (m/s)	15
Total hoisted mass M (kg)	17 584
Sheave wheel moment of inertia I (kg/m^2)	15 200
Winder drum radius R_d (m)	2.14
Sheave wheel radius R (m)	2.13
Coil cross-over arc β (rad)	0.2
Cable diameter d (m)	48×10^{-3}
Cable linear density (kg/m)	8.4
Cable effective steel area A (m)^2	1.028×10^{-3}
Cable effective Young's Modulus E (N/m^2)	1.1×10^{11}
Catenary length L_c (m)	74.95
Maximum depth of winding $L_{v\,max}$ (m)	2100
Lateral modal damping ratio ζ (%)	0.05
Relative damping coefficient μ_1 (s)	Given by Eq. (14)
Absolute damping coefficient μ_2 (s^{-1})	0.159

with respect to the fast time scale (T). Furthermore, $\mathbf{A}(T,\tau;\varepsilon)$ is a $2(2N_{lat}+N_{long})\times 2(2N_{lat}+N_{long})$-dimensional slowly varying (non-stationary) state matrix, $\mathbf{N}(\tau,\mathbf{y})$ represents the $2(2N_{lat}+N_{long})$-dimensional vector of non-linear coupling terms, and $\mathbf{F}(T,\tau)$ is the $2(2N_{lat}+N_{long})$-dimensional external excitation vector.

The non-stationary state matrix is given as

$$\mathbf{A} = (T,\tau;\varepsilon) = \begin{bmatrix} \mathbf{0} & \mathbf{I} \\ -\mathbf{K}(T,\tau) & -\mathbf{C}(\tau;\varepsilon) \end{bmatrix}, \tag{2}$$

where $\mathbf{0}$ and $\mathbf{I}$ are $(2N_{lat}+N_{long})\times(2N_{lat}+N_{long})$ null and identity matrices, respectively, and $\mathbf{K}$ and $\mathbf{C}$ are $(2N_{lat}+N_{long})\times(2N_{lat}+N_{long})$ matrices. These matrices are defined as

$$\mathbf{K}(T,\tau) = \begin{bmatrix} \mathbf{K}^{lat}(T,\tau) & \mathbf{0} & \mathbf{0} \\ \mathbf{0} & \mathbf{K}^{lat}(T,\tau) & \mathbf{0} \\ \mathbf{0} & \mathbf{0} & \mathbf{K}^{long}(\tau) \end{bmatrix}, \tag{3}$$

$$\mathbf{C}(\tau;\varepsilon) = \begin{bmatrix} \mathbf{C}^{lat}(\tau;\varepsilon) & \mathbf{0} & \mathbf{0} \\ \mathbf{0} & \mathbf{C}^{lat}(\tau;\varepsilon) & \mathbf{0} \\ \mathbf{0} & \mathbf{0} & \mathbf{C}^{long}(\tau;\varepsilon) \end{bmatrix}, \tag{4}$$

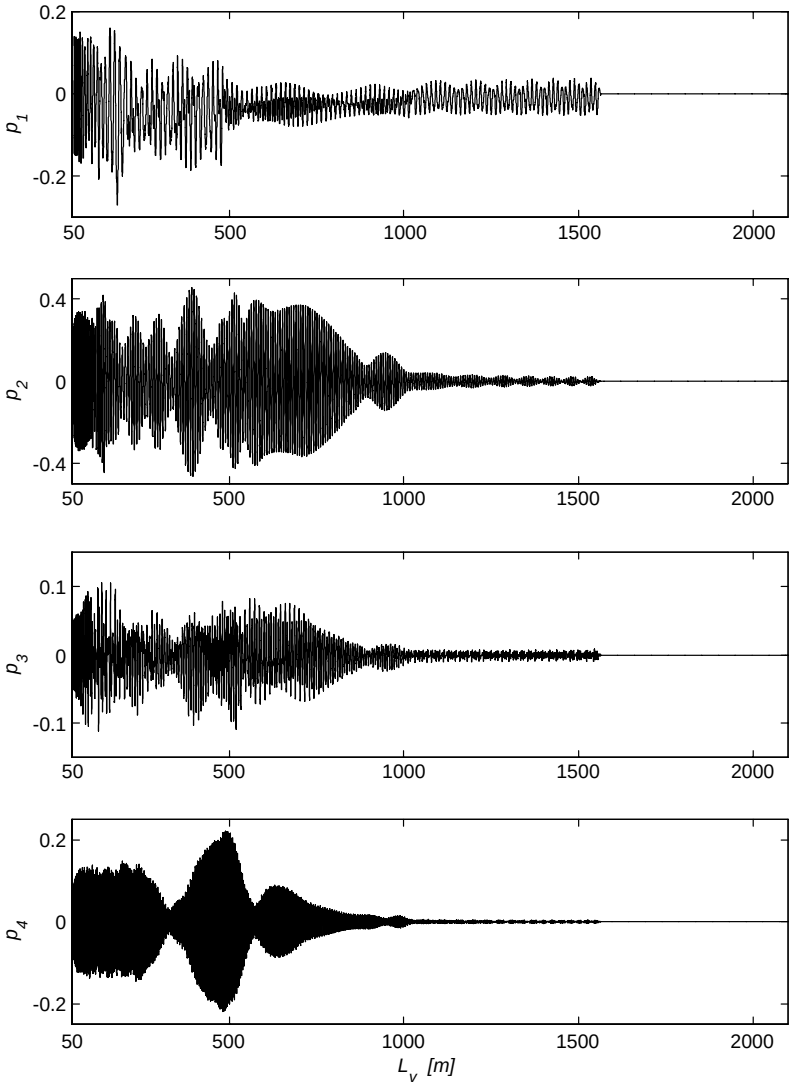

Fig. 3. Plots of the lateral in-plane modal co-ordinates, $V_c = 15\,\mathrm{m/s}$.

where $\mathbf{K}^{lat}$, $\mathbf{C}^{lat}$ are $N_{lat} \times N_{lat}$ matrices, and $\mathbf{K}^{long}$, $\mathbf{C}^{long}$ are $N_{long} \times N_{long}$ matrices. When terms $O(\varepsilon^2)$ are neglected, these matrices are determined as

$$\mathbf{K}^{lat}(T,\tau) = \left[1 + \left(\frac{c}{\bar{c}}\right)^2 F_l(T)\right] \mathrm{diag}[\hat{\omega}_k^2(\tau)], \tag{5}$$

$$\mathbf{C}^{lat}(\tau;\varepsilon) = [C_{kn}^{lat}] = 2\varepsilon\left\{\mathrm{diag}[\bar{\zeta}_k^* \hat{\omega}_k(\tau)] + \frac{2l'}{mL_c}[C_{kn}]\right\}, \tag{6}$$

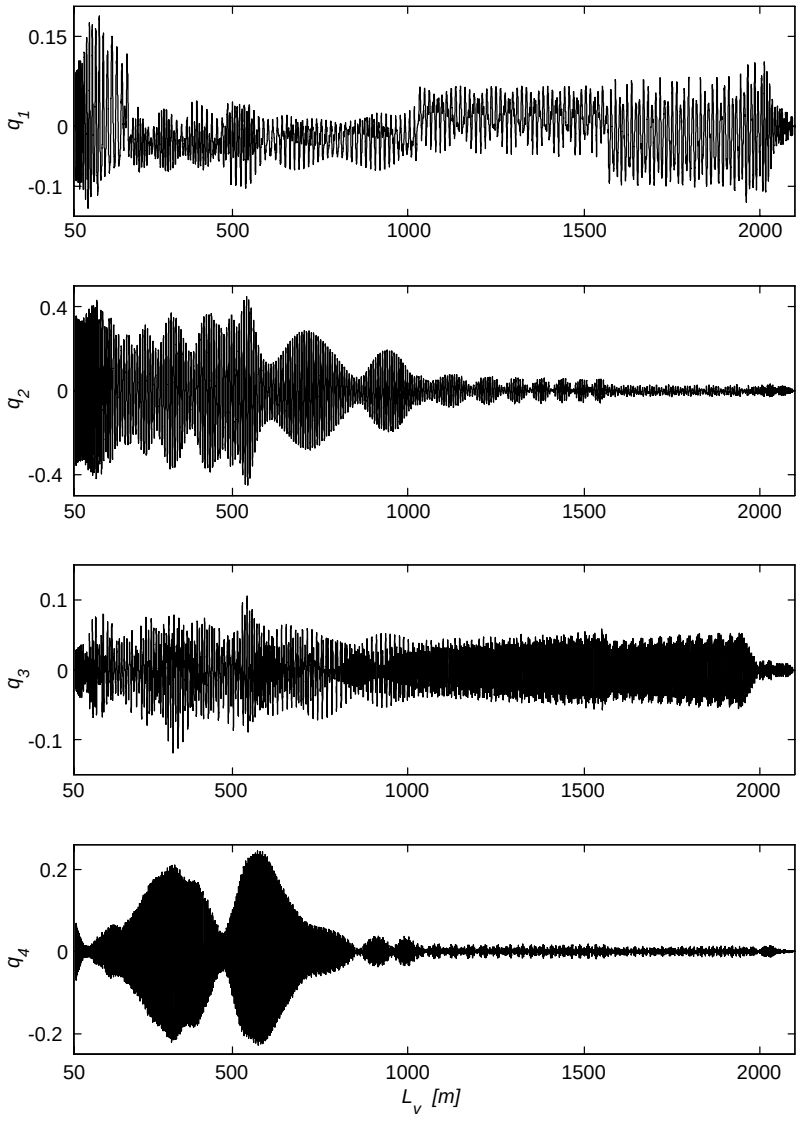

Fig. 4. Plots of the lateral out-of-plane modal co-ordinates, $V_c = 15\,\mathrm{m/s}$.

$$\mathbf{K}^{long}(\tau) = \mathrm{diag}[\tilde{\omega}_\tau^2(\tau)], \tag{7}$$

$$\mathbf{C}^{long}(\tau;\varepsilon) = [C_{rn}^{long}] = \varepsilon\frac{\mu_2^*}{\omega_0}\mathbf{I} + \frac{\varepsilon}{m_r^v(\tau)}\left[2l' C_{rn}^v(\tau) - \frac{EA}{\omega_0}\Lambda_{rn}^* + M_S l'\left(\frac{1}{L_c} - \frac{M_S}{m}\gamma_n^2\right)\right], \tag{8}$$

where $\mathbf{I}$ is a $\mathbf{N}_{long} \times \mathbf{N}_{long}$ identity matrix. Next, the non-linear vector $\mathbf{N}(\tau, \mathbf{y})$ is given as

$$\mathbf{N}^v(\tau, \mathbf{y}) = \left[\mathbf{0}_{[1\times(2N_{lat}+N_{long})]}, \quad \mathbf{N}^{v\mathrm{T}}(\tau, \mathbf{y}), \quad \mathbf{N}^{w\mathrm{T}}(\tau, \mathbf{y}) \quad \mathbf{N}^{u\mathrm{T}}(\tau, \mathbf{y})\right]^{\mathrm{T}}, \tag{9}$$

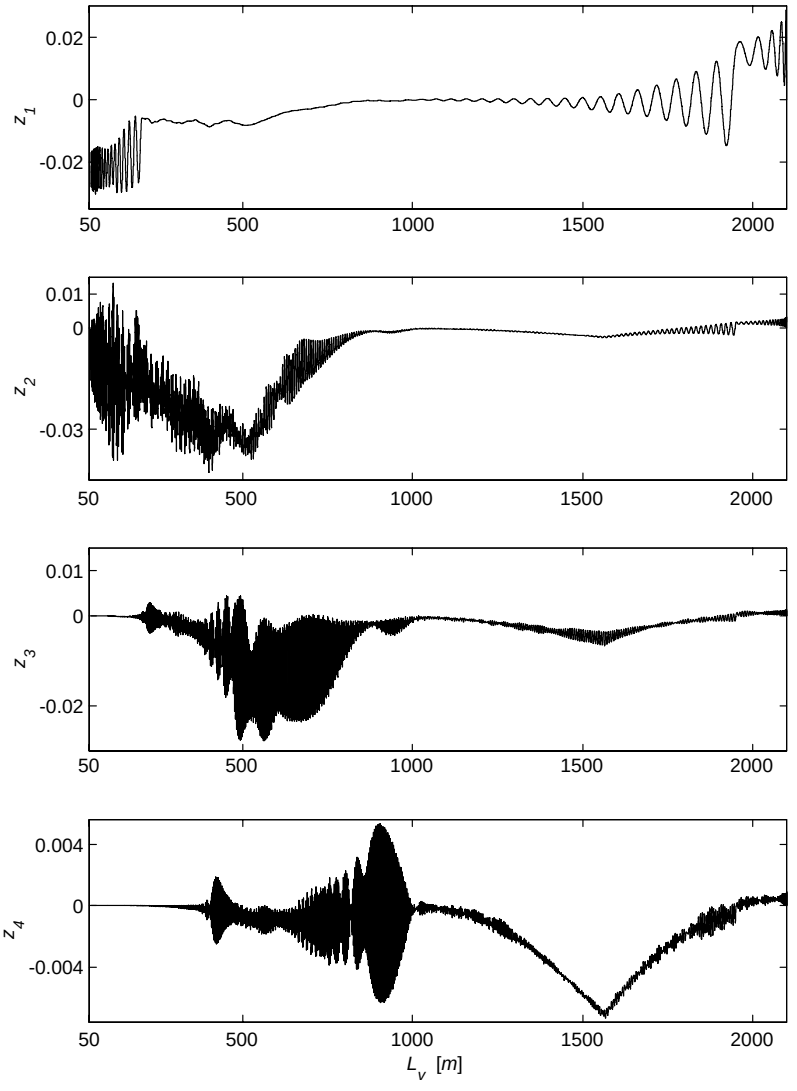

Fig. 5. Plots of the longitudinal modal co-ordinates, $V_c = 15\,\mathrm{m/s}$.

where

$$\mathbf{N}^v(\tau,\mathbf{y}) = [N_k^v]_{(N_{lat}\times 1)} = -\left(\frac{c}{\bar{c}}\right)^2 \left\{ \hat{\omega}_k^2(\tau)\left[\frac{1}{L_c}\sum_{n=1}^{N_{long}} z_n + \sum_{n=1}^{N_{lat}} \beta_n^2(p_n^2+q_n^2)\right] p_k \right\}, \tag{10}$$

$$\mathbf{N}^w(\tau,\mathbf{y}) = [N_k^w]_{(N_{lat}\times 1)} = -\left(\frac{c}{\bar{c}}\right)^2 \left\{ \hat{\omega}_k^2(\tau)\left[\frac{1}{L_c}\sum_{n=1}^{N_{long}} z_n + \sum_{n=1}^{N_{lat}} \beta_n^2(p_n^2+q_n^2)\right] q_k \right\}, \tag{11}$$

$$\mathbf{N}^u(\tau,\mathbf{y}) = [N_r^u]_{(N_{long}\times 1)} = -\frac{EA}{\omega_0^2}\left[\frac{1}{m_r^v(\tau)}\sum_{n=1}^{N_{lat}} \beta_n^2(p_n^2+q_n^2)\right]. \tag{12}$$

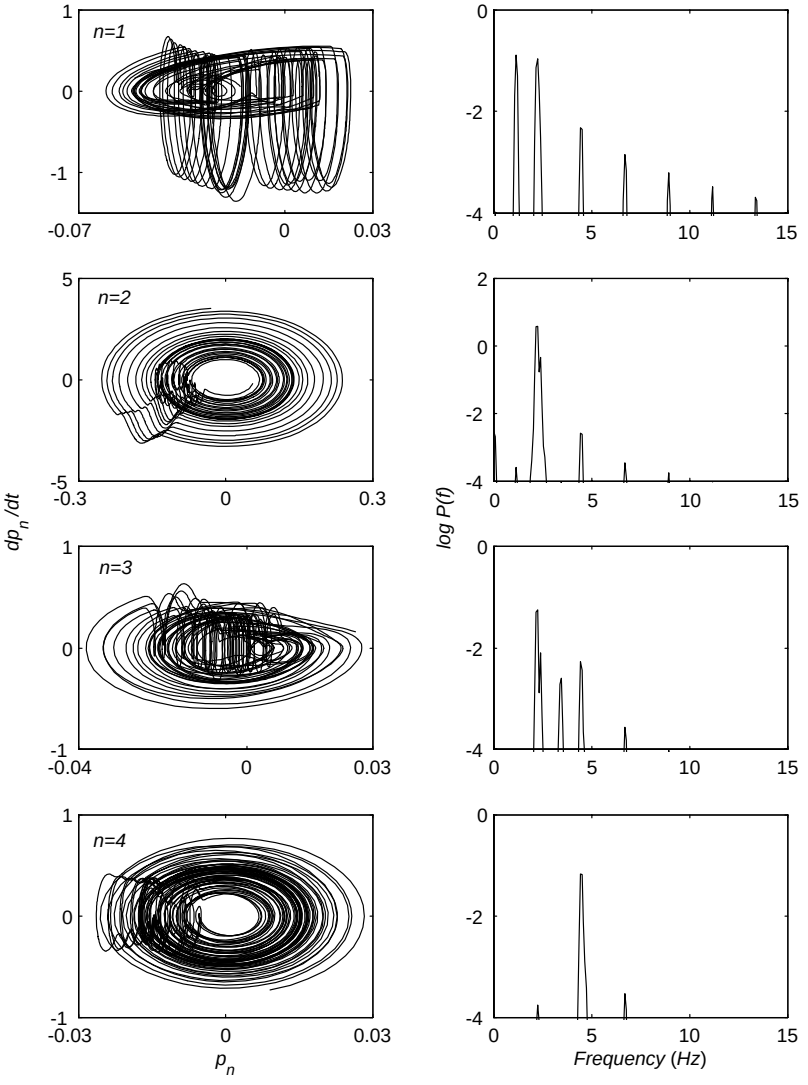

Fig. 6. Phase space trajectories and associated power spectra at each successive layer, n, starting at layer 1 in the top row to layer 4 in the bottom row: the lateral in-plane modal co-ordinates, $V_c = 15\,\mathrm{m/s}$, $L_v = 1000$–$800\,\mathrm{m}$.

Lastly, the excitation vector $\mathbf{F}$ is given in the form

$$\mathbf{F}(\tau, T) = \begin{bmatrix} \mathbf{0}_{[(2N_{lat}+2N_{long})\times 1]} \\ \begin{bmatrix} \hat{P}_r \\ \hat{Q}_r \\ \hat{Z}_r - \dfrac{EA}{m_r^v} F_l(T) \end{bmatrix}_{[(2N_{lat}+N_{long})\times 1]} \end{bmatrix}. \tag{13}$$

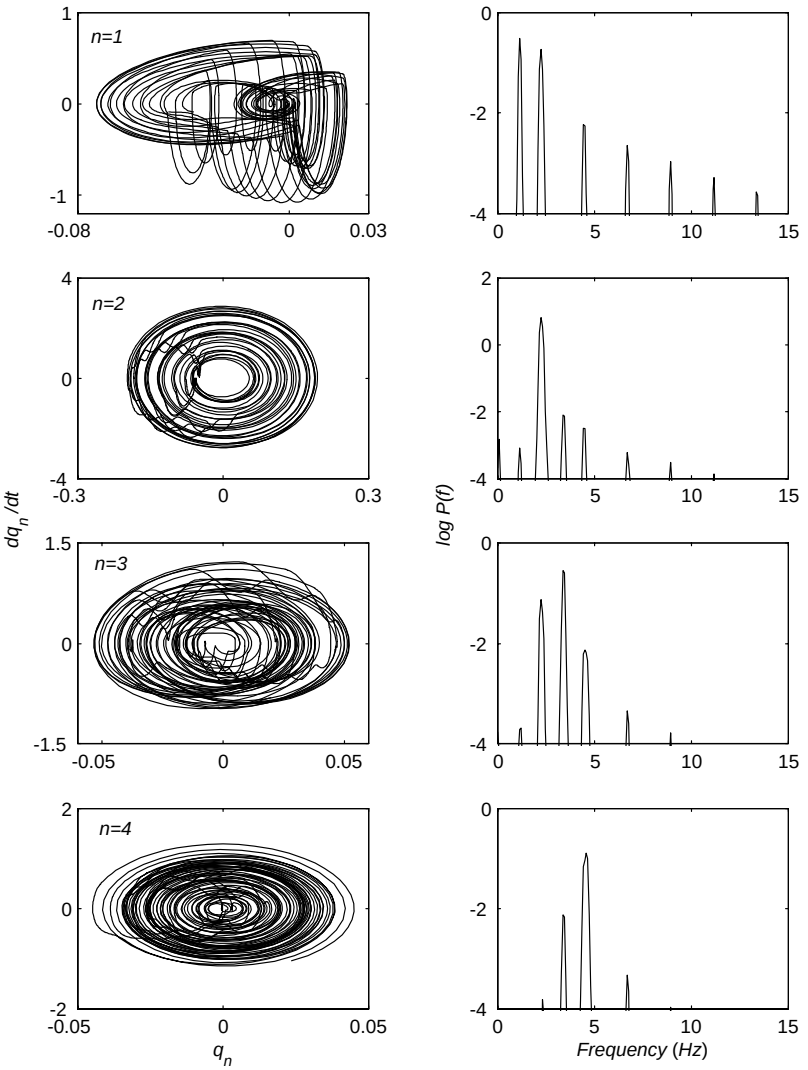

Fig. 7. Phase space trajectories and associated power spectra for successive layers as in Fig. 6: the lateral out-of-plane modal co-ordinates, $V_c = 15$ m/s, $L_v = 1000$–800 m.

2.2. Identification of the cable damping parameters

The equivalent proportional viscous damping has been assumed in the non-linear model to represent both the lateral and longitudinal overall damping effort in the system [3]. In the longitudinal damping model, the damping coefficient μ_1, being part of the coefficient Λ^*_{rn} in Eq. (8) represents internal damping effects, that are proportional to the rate of strain in the cable, and the second damping coefficient μ_2 accommodates the external damping in the system.

The coefficient μ_1 is usually assumed to be a function of some cable parameters, which may be established from an appropriate experiment. Goroshko and Savin [4] showed that this coefficient

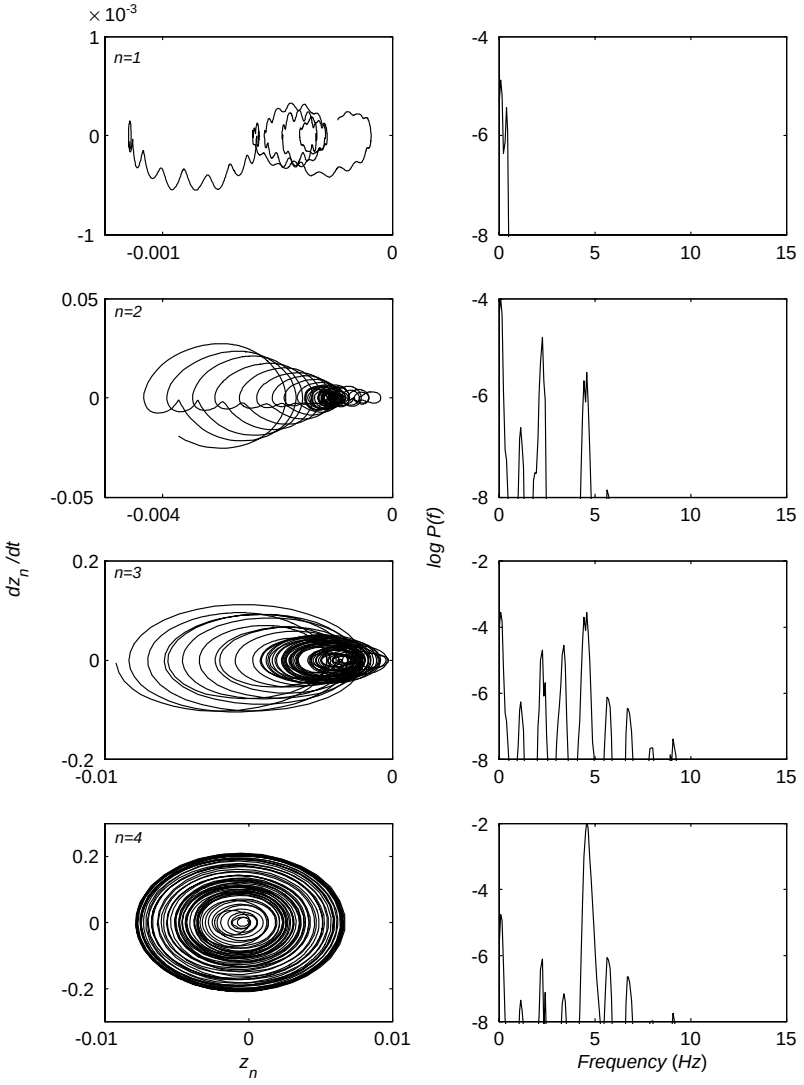

Fig. 8. Phase space trajectories and associated power spectra for successive layers as in Fig. 6: the longitudinal modal co-ordinates, $V_c = 15$ m/s, $L_v = 1000$–800 m.

is independent of the amplitude of oscillations in the cable dynamic tension, but depends on the mean (quasi-static) value of the cable tension. Namely, μ_1 decreases with increasing mean tension. This effect was also observed by Mankowski and Cox [5]. It can be argued that when the tension is increased, the wire strands are more readily locked, and the inter-strand relative motion is constrained, resulting in the coefficient μ_1 being decreased. This agrees with an earlier observation by Vanderveldt and Gilheany [6] who found that the velocity of propagation of a longitudinal pulse in wire ropes increases with increasing applied tension load, and postulated that this was due to the cable approaching the geometry of a solid bar due to a gradual tightening of the wires and

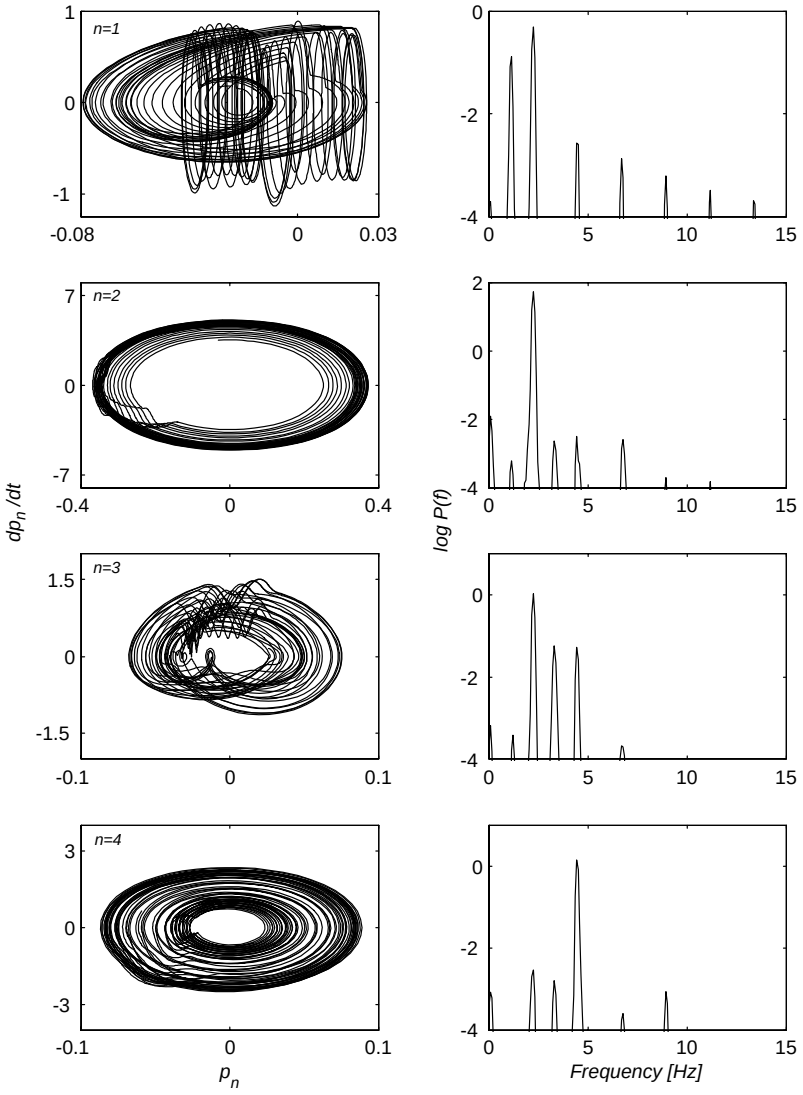

Fig. 9. Phase space trajectories and associated power spectra for successive layers as in Fig. 6: the lateral in-plane modal co-ordinates, $V_c = 15$ m/s, $L_v = 800$–600 m.

strands. Constancon [7] analyzed the results of damping measurements via drop tests. In these tests, a conveyance was clamped between the guides, loaded with a dead weight, and released. The response was monitored with an accelerometer, and the modal damping ratios were extracted from the measurements using standard parameter estimation procedures. A strong dependency of the fundamental mode damping ratio on the mean rope tension was recorded. It was evident that the damping ratio decreased approximately linearly with the tension.

Taking into account the existing strong evidence, the dependency of the damping coefficient μ_1 on the mean tension is accommodated in the present analysis and the damping coefficient is

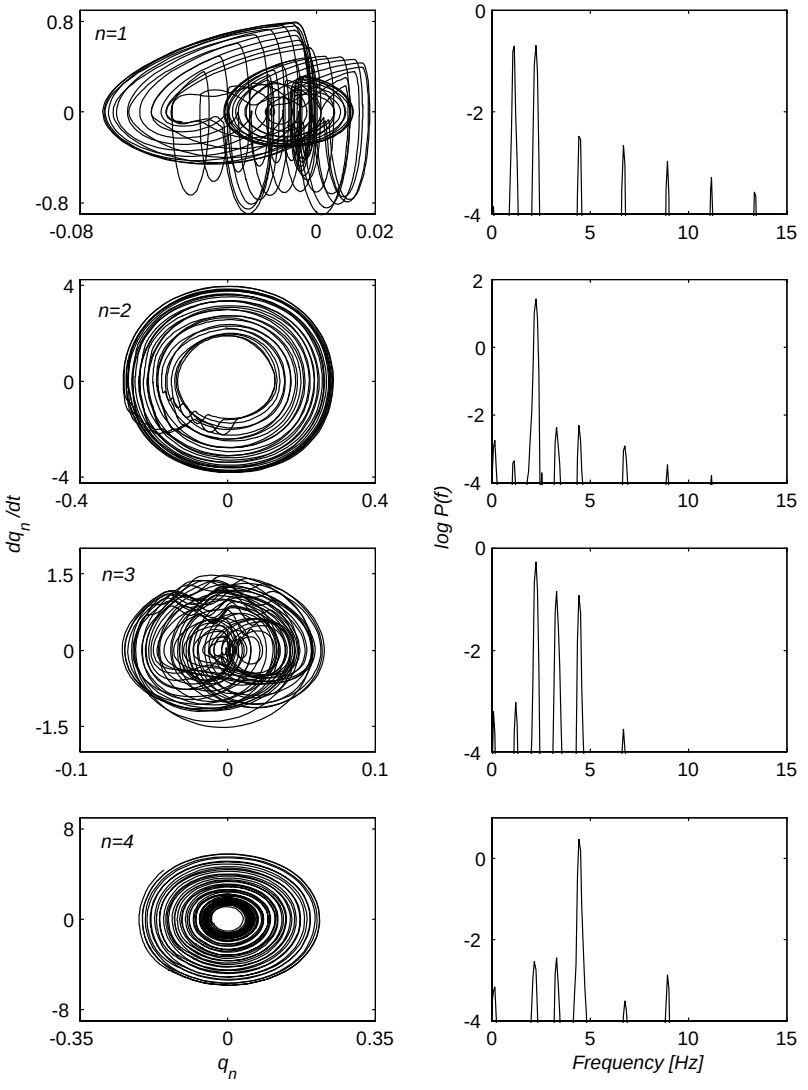

Fig. 10. Phase space trajectories and associated power spectra for successive layers as in Fig. 6: the lateral out-of-plane modal co-ordinates, $V_c = 15\,\mathrm{m/s}$, $L_v = 800$–$600\,\mathrm{m}$.

defined as [8]

$$\mu_1 = \left(0.5 + \frac{23000}{3500 + 0.75 \times 10^{-5}\sigma_v^i}\right) \times 10^{-4}, \tag{14}$$

where σ_v^i denotes the mean stress in the cable in $\mathrm{N/m^2}$, and is given as $\sigma_v^i = T_v^i/A$, where T_v^i denotes the slowly varying mean tension in the vertical rope.

As already mentioned, the external damping effects, such as air damping, friction at conveyance guides, and damping at the sheave wheel bearings, are represented by the coefficient μ_2. The order

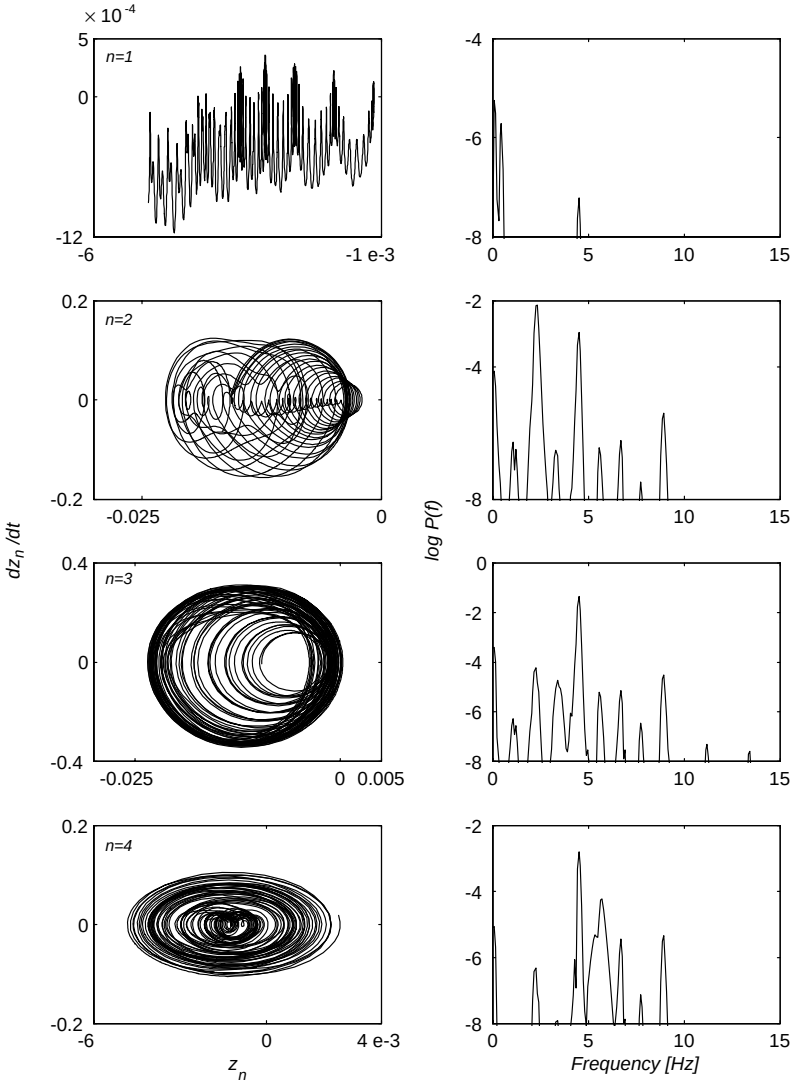

Fig. 11. Phase space trajectories and associated power spectra for successive layers as in Fig. 6: the longitudinal modal co-ordinates, $V_c = 15\,\text{m/s}$, $L_v = 800$–$600\,\text{m}$.

of this coefficient was established by the results of drop tests [7], and the coefficient values were estimated to range from 0.159 to $0.1797\,\text{s}^{-1}$.

The correct choice of the cable lateral damping parameters must also be addressed in more detail. This problem attracted much attention from researchers in the area of wire cable mechanics. The basic nature of internal damping in stranded structural cables and its influence on transverse vibration was studied by Yu [9]. In this study, static and dynamic experimental tests on 7-wire cable specimens were performed, from which the deformation and energy relationships were developed. It was established that interstrand dry

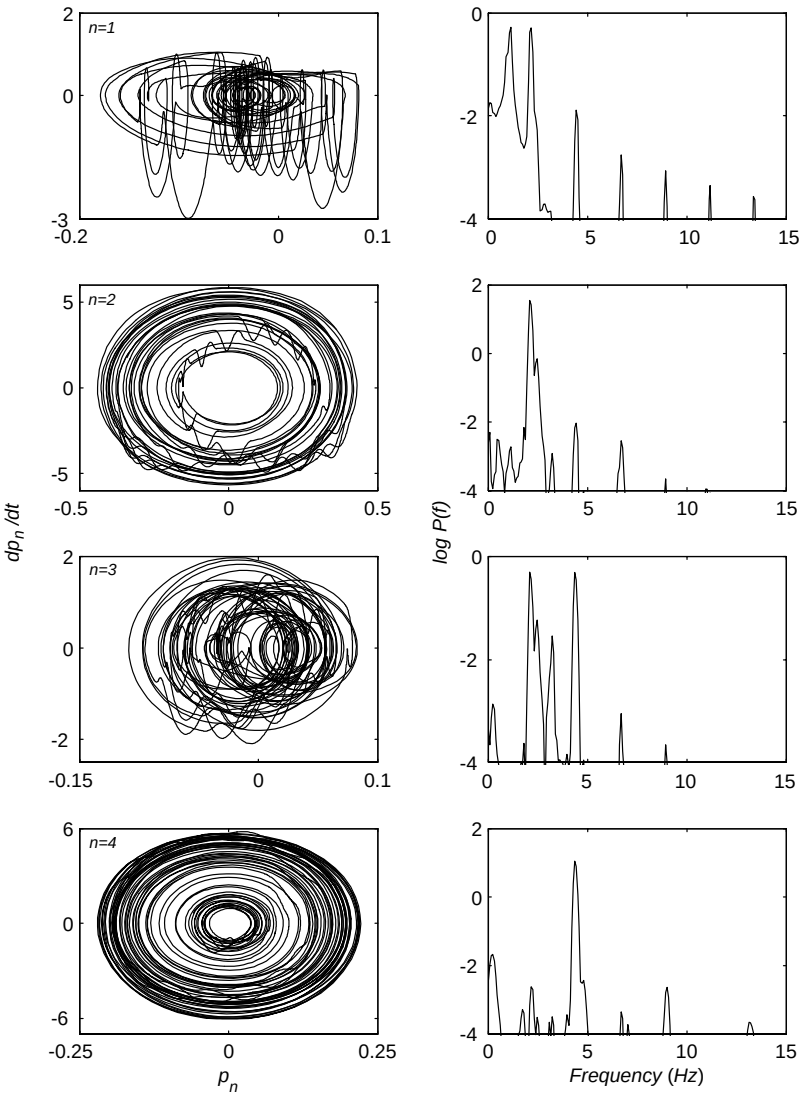

Fig. 12. Phase space trajectories and associated power spectra for successive layers as in Fig. 6: the lateral in-plane modal co-ordinates, $V_c = 15$ m/s, $L_v = 600$–400 m.

friction is the main source of internal damping in wire cables, and energy dissipation per cycle (damping capacity) is a linear function of amplitude. Factors that may influence internal damping were also identified. Namely the test results indicated the increase of damping capacity with the reduction of lay length, and with the increase of number of wires in strands of comparable sizes. Furthermore, the reduction of the damping capacity with prestressing of cables over yield point was recorded. It was also shown that cables with wires in which the twist was formed before they were stranded together (preformed cables) possessed less damping capacity than non-preformed ones.

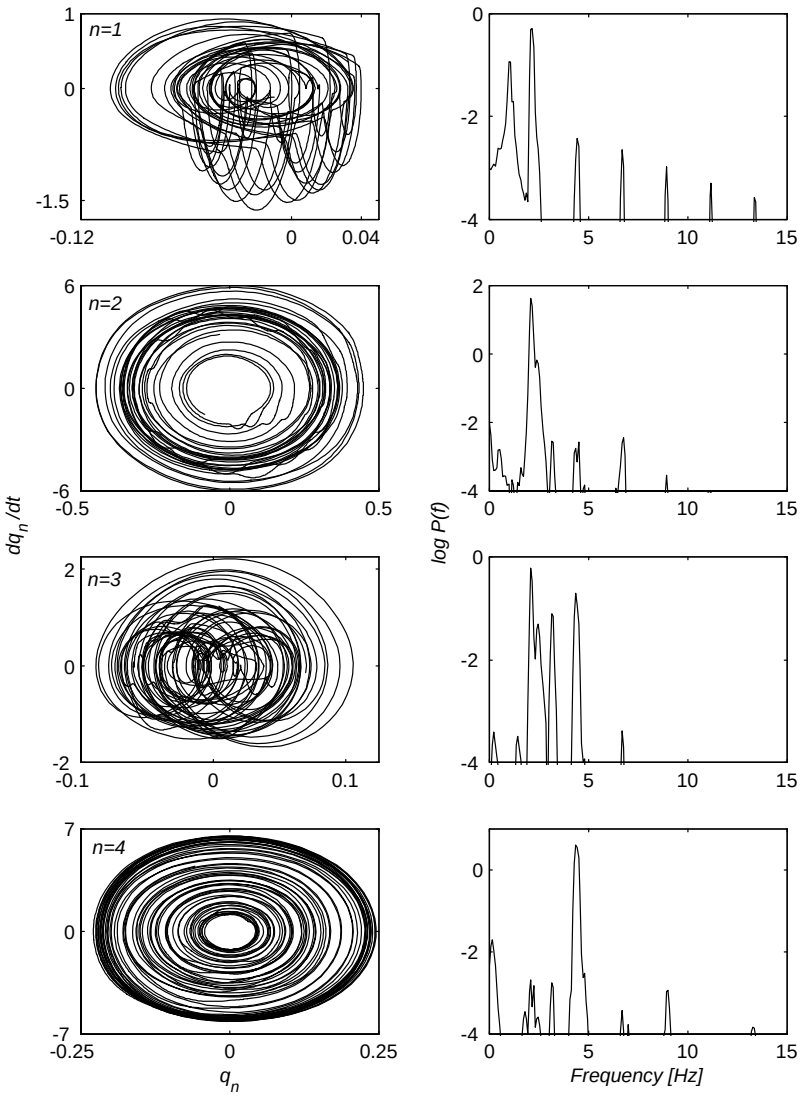

Fig. 13. Phase space trajectories and associated power spectra for successive layers as in Fig. 6: the lateral out-of-plane modal co-ordinates, $V_c = 15$ m/s, $L_v = 600$–400 m.

Vanderveldt et al. [10] also conducted damping studies in wire ropes of various types, and determined the lateral equivalent viscous damping coefficient from measurements of the logarithmic decrement. The results of this investigation showed that the damping coefficient increases with increasing axial load applied to the rope. It was concluded that this increasing tensile load contributes to the friction effects between individual wires and strands, and that Coulomb damping is responsible for a major portion of the equivalent damping coefficient. Furthermore, it was also established that the geometry and construction of a wire rope has a significant influence on the damping coefficient.

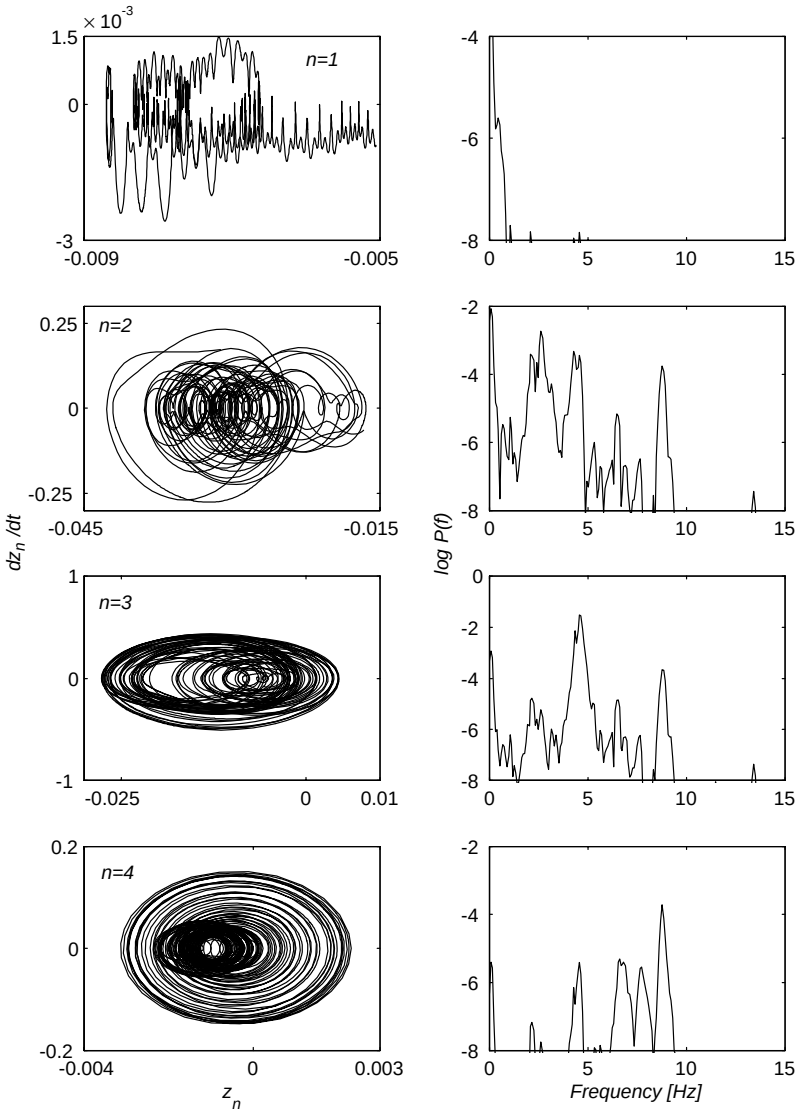

Fig. 14. Phase space trajectories and associated power spectra for successive layers as in Fig. 6: the longitudinal modal co-ordinates, $V_c = 15$ m/s, $L_v = 600$–400 m.

Irvine [11] studied the dynamic response of flat-sag suspended cable making provision for lateral viscous damping through modal damping, introduced in the discrete model of the cable. He stated that the internal damping in wire cables is affected by the lay of the strands and is usually small, resulting due to rubbing between individual wires. He quoted also that the internal damping could be expected to be larger in slack cables rather than in taut cables, with the corresponding damping ratios $\zeta = 4\%$ and 0.4%, respectively. The air (external) damping was identified as negligible in still air, but as contributing substantially to the energy dissipation in strong winds, with the suggested damping ratio up to $\zeta = 4\%$.

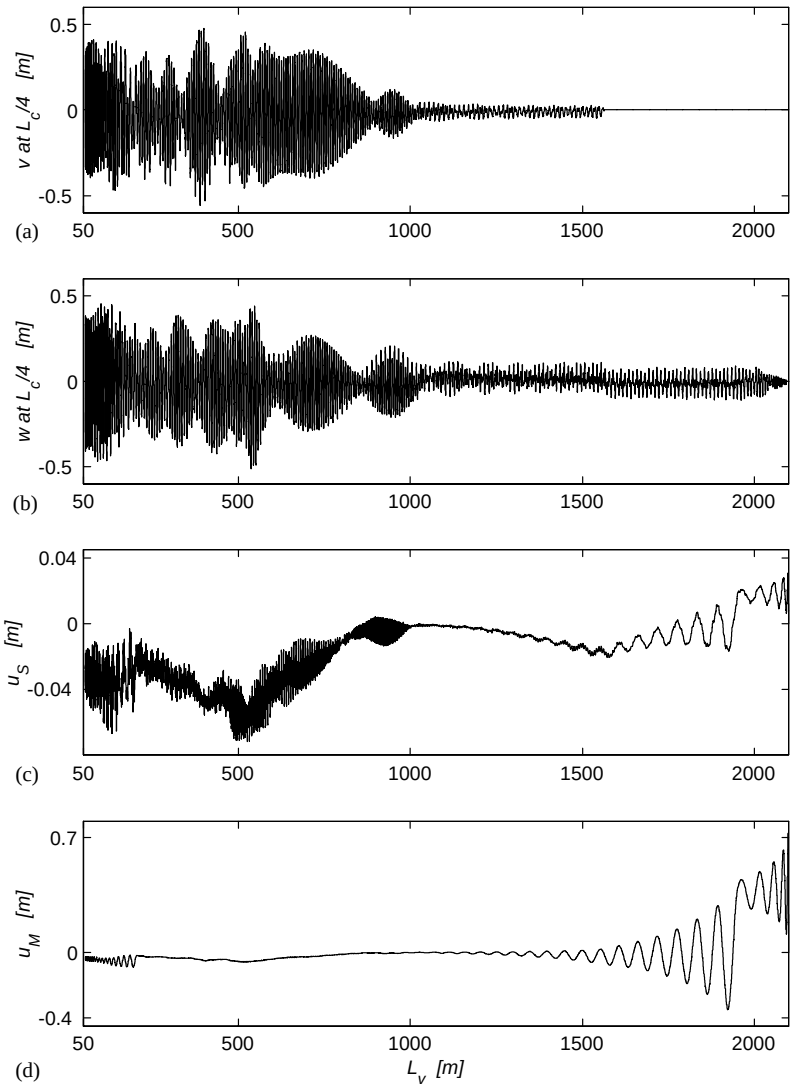

Fig. 15. Displacement response plots for $V_c = 15\,\mathrm{m/s}$: lateral (a) in-plane motions and (b) out-of-plane motions at the first quarter of the catenary; longitudinal responses (c) at the sheave and (d) at the conveyance.

Mankowski [12] proposed an empirical formula for quantifying the damping mechanism occurring in mine hoisting cables undergoing non-planar lateral motion. He expressed the power dissipation in terms of the amplitude and frequency of vibration, the cable span, and two experimentally determined coefficients, namely the damping capacity coefficient, and the curvature characteristic. A mathematical relationship was developed that enabled the amount of internal power loss due to damping to be assessed. Furthermore, it was established that a critical cable curvature exists above which the internal power loss increased linearly with increasing amplitude-to-span ratio. The results of this research were extended and applied to

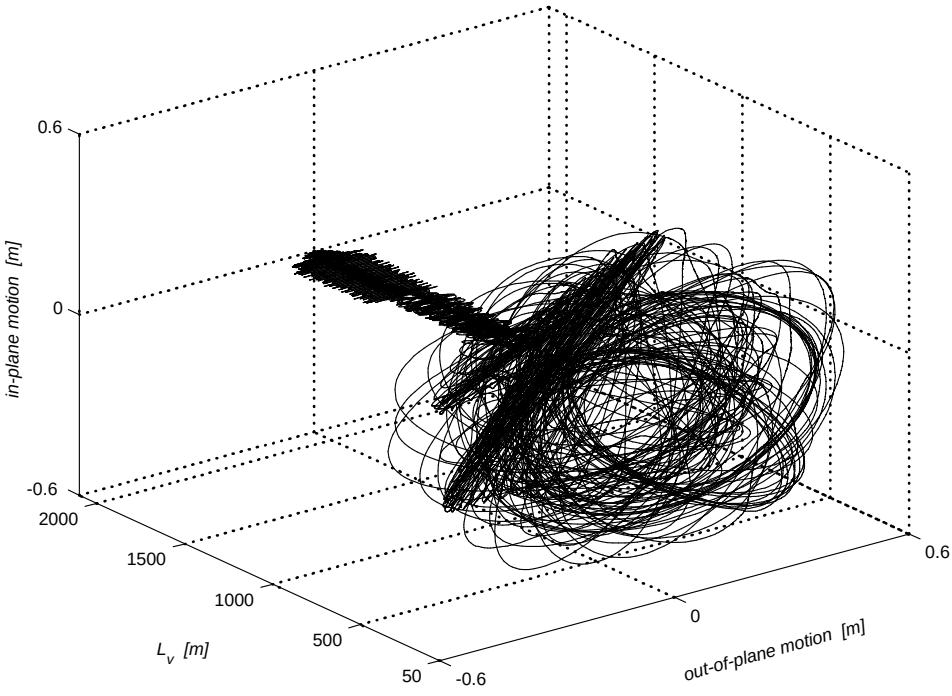

Fig. 16. Lateral cable motion at the first quarter point of the catenary at $V_c = 15\,\mathrm{m/s}$.

assess the effects of internal friction occurring at the wavefront of travelling transverse disturbances on mine hoisting cable [13].

Constancon [7] used this damping model and converted Mankowski's results into equivalent viscous damping coefficients, and consequently determined the corresponding equivalent damping ratios ζ, which were identified to be very small, namely ranging from 0.007% to 0.017%. He indicated that aerodynamic effects may be significant in the lateral damping mechanism, and determined the corresponding equivalent viscous damping coefficients in terms of the air density, cable diameter and span, and the amplitude and frequency of vibration. The corresponding damping ratios were calculated for the same parameters as used by Mankowski, and were found to be between 0.04% and 0.1%.

Due to the lack of any other reliable lateral damping data, Mankowski's test results are used as the basis for the lateral damping model in the present analysis. Consequently, the lateral damping is represented by ratios $\bar{\zeta}_r$ in the equations of motion.

2.3. Cross-over excitation definition

A periodic excitation resulting from the cross-over cable motion on the drum is imparted to the system during the winding cycle as discussed in more detail in Part 1 [3]. This excitation is represented by functions $v_l(t)$, $w_l(t)$ and $u_l(t)$. The lateral out-of-plane excitation w_l occurs due to a transverse motion of the cable in the cross-over zone across the drum through a distance of a half its diameter, relative to the entry position. As multiple layers are required

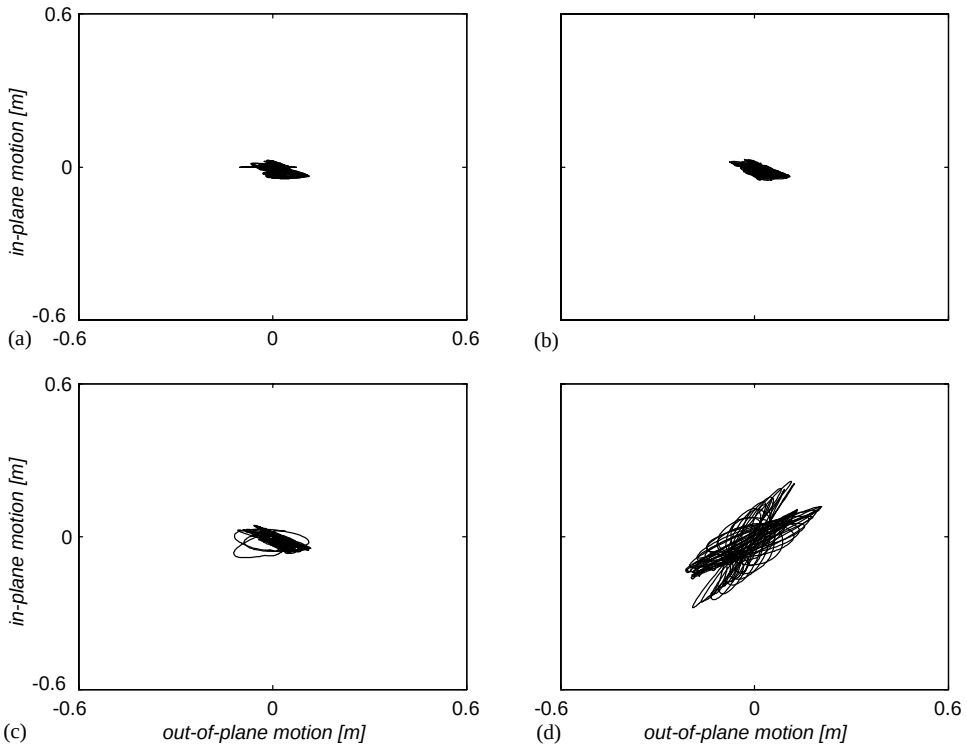

Fig. 17. The trajectory of the first quarter point of the catenary during various stages of the ascending cycle at $V_c = 15\,\mathrm{m/s}$: (a) $L_v = 1600-1400\,\mathrm{m}$, (b) $L_v = 1400-1200\,\mathrm{m}$, (c) $L_v = 1200-1000\,\mathrm{m}$, (d) $L_v = 1000–800\,\mathrm{m}$.

to wind the cable, the direction of this motion is reversed after the layer change which represents a 180° phase shift in the excitation relative to that of the previous layer. The cross-over excitation v_1 in the lateral in-plane direction takes place on the second and higher layers, and represents a radial shift of the cable over underlying coils of the previous layer. An additional axial displacement relative to the nominal transport motion is also applied to the cable in the cross-over region. This is a consequence of the increase in the axial velocity of the cable to compensate for the difference between the arc length covered through a cross-over, and that which would be covered without a cross-over. This effect is represented by the excitation component u_l.

These excitation functions can be defined in terms of the geometry of the system and the transport velocity. Mankowski [14] proposed a definition by means of versine functions. During the constant velocity phase the excitation functions are given by the equations from Ref. [2]

$$v_l = \left\{ \begin{array}{ll} \frac{1}{2}v_0^n[1-\cos(2\nu t)], & 0 \leqslant t \leqslant t_\beta \\ 0, & t_\beta \leqslant t \leqslant \tau_e \end{array} \right\}, \tag{15}$$

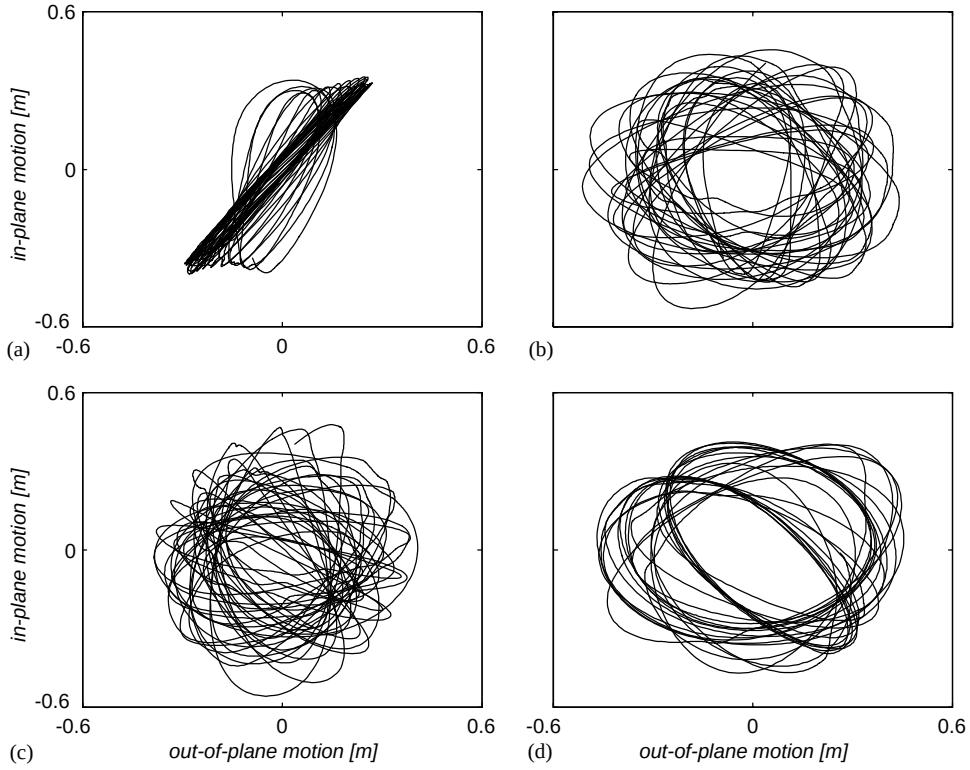

Fig. 18. The trajectory of the first quarter point of the catenary during various stages of the ascending cycle at $V_c = 15\text{m/s}$: (a) $L_v = 800-600\,\text{m}$, (b) $L_v = 600-400\,\text{m}$, (c) $L_v = 400–150\,\text{m}$, (d) $L_v = 150–60\,\text{m}$.

$$w_l = \begin{cases} \frac{1}{2}w_0[1-\cos(vt)], & 0 \leqslant t \leqslant t_\beta \\ \dfrac{d}{2}, & t_\beta \leqslant t \leqslant \tau_e \end{cases}, \tag{16}$$

$$w_l = \begin{cases} \frac{1}{2}u_0[1-\cos(vt)], & 0 \leqslant t \leqslant t_\beta \\ u_0(\tau - t)/(\tau_e - \tau_\beta), & t_\beta \leqslant t \leqslant \tau_e \end{cases}, \tag{17}$$

where v_0, w_0 and u_0 are determined from the geometry of the cross-over as

$$v_0^n = (n-1)\left(1 - \frac{\sqrt{3}}{2}\right)d, \quad n = 1,2,3,4, \qquad w_0 = \frac{d}{2}, \tag{18,19}$$

$$u_0 = R_d\beta\left[\sqrt{1 + \left(\frac{d}{2R_d\beta}\right)^2 + \left(\frac{2v_0^n}{R_d\beta}\right)^2} - 1\right], \tag{20}$$

in which n denotes the layer number, d is the cable diameter, R_d is the drum radius, β is the angle defining the cross-over diametrical arc, and where $t_\beta = \beta/\omega_d$, with $\omega_d = V_c/R_d$, represents the

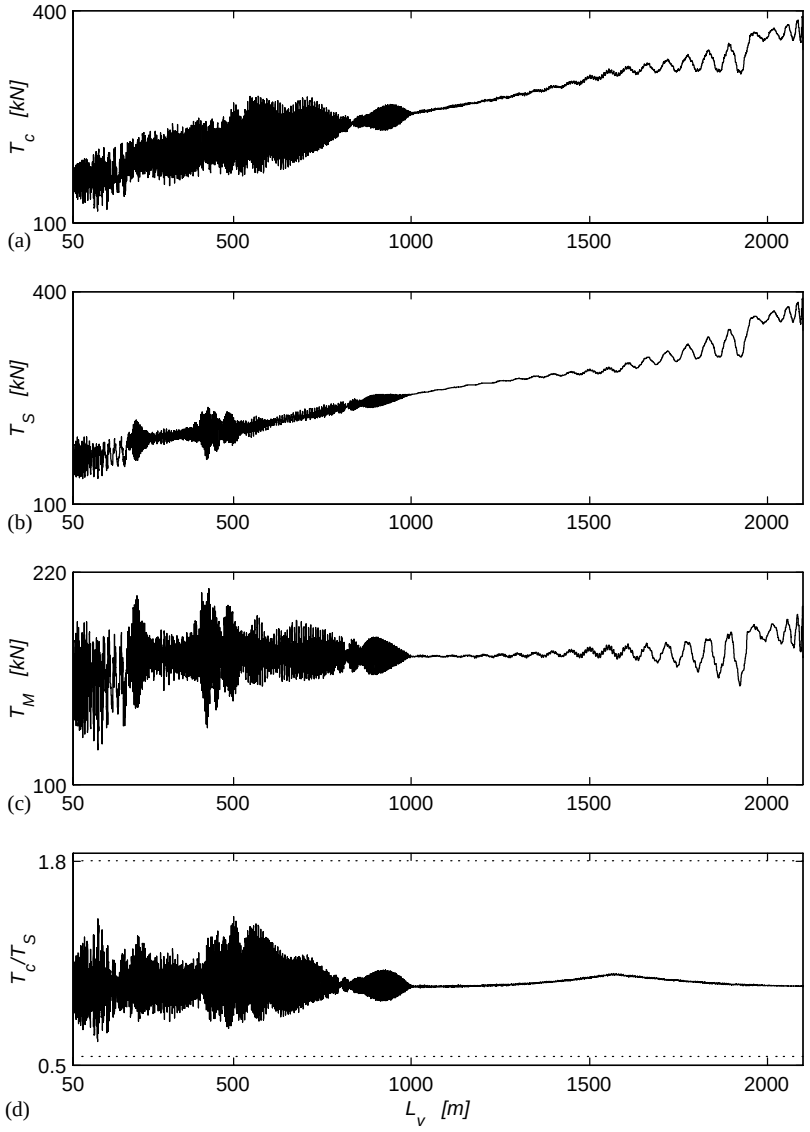

Fig. 19. Total tensions in the winding cables at the nominal velocity $V_c = 15\,\mathrm{m/s}$: (a) the catenary tension T_c; (b) the vertical rope tension T_S at the sheave; (c) the vertical rope tension T_M at the conveyance; and (d) the tension ratio across the sheave T_c/T_S.

duration of the cross-over pulse, $\tau_e = 2\pi/\Omega$, where $\Omega = 2\omega_d$, is the period of the excitation, V_c denotes the nominal transport velocity, and $v = \pi/t_\beta$. The cross-over excitation functions for typical parameter values of $d = 0.048\,\mathrm{m}$, $R_d = 2.14\,\mathrm{m}$, $V_c = 15\,\mathrm{m/s}$, and $\beta = 0.2\,\mathrm{rad}$ are shown in Fig. 1. It can be noted that the most significant is the excitation in the lateral out-of-plane direction which is an order of magnitude larger than the lateral in-plane pulse. The axial (longitudinal) pulse is an order of magnitude smaller than the in-plane pulse. However, the rope

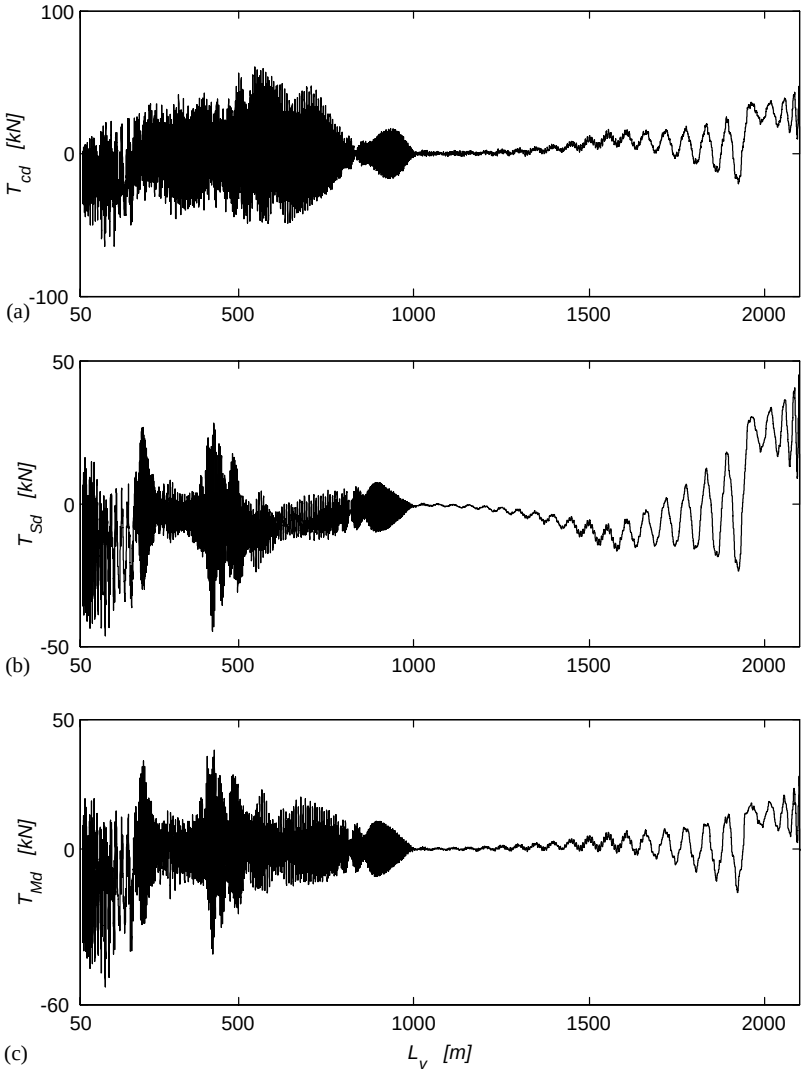

Fig. 20. Dynamic tensions in the winding cables at the nominal speed $V_c = 15\,\mathrm{m/s}$: (a) the catenary dynamic tension T_{cd}; (b) the vertical rope dynamic tension T_{Sd} at the sheave; and (c) the vertical rope dynamic tension T_{Md} at the conveyance.

longitudinal stiffness is high and large axial tensions, of the order of 5 kN [15], can arise in the rope due to the longitudinal pulse.

3. Simulation results

Typical parameters of a double-drum Blair multi-rope (BMR) system with two conveyances (skips) attached via compensating sheaves on bridles are chosen to carry out numerical

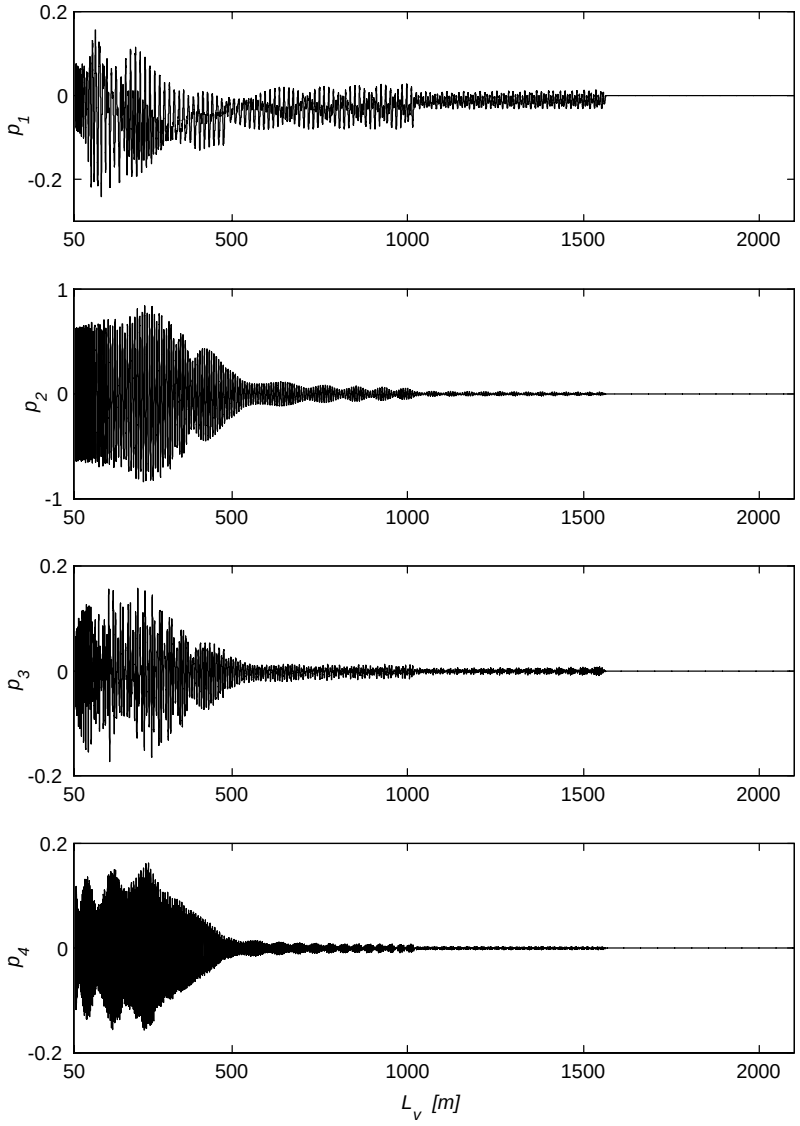

Fig. 21. Plots of the lateral in-plane modal co-ordinates, $V_c = 14\,\mathrm{m/s}$.

simulation of the system described by Eq. (1). A schematic diagram showing the arrangement of cables in this system is presented in Fig. 2. In this installation, the underlay cable 1 wound onto the underlay drum D_1 passes over the headsheaves H_1 and H_2 and supports the underlay skip S_1, forming two catenary sections and two vertical ropes. Similarly, two catenaries and vertical ropes are formed by the overlay cable 2 wound onto the overlay drum D_2 and supporting the overlay skip S_2. The fundamental parameters of this system are displayed in Table 1.

A single overlay, or underlay, arrangement with one conveyance is analyzed in what follows. In this model, an equivalent catenary and an equivalent vertical rope, supporting one-half of the full

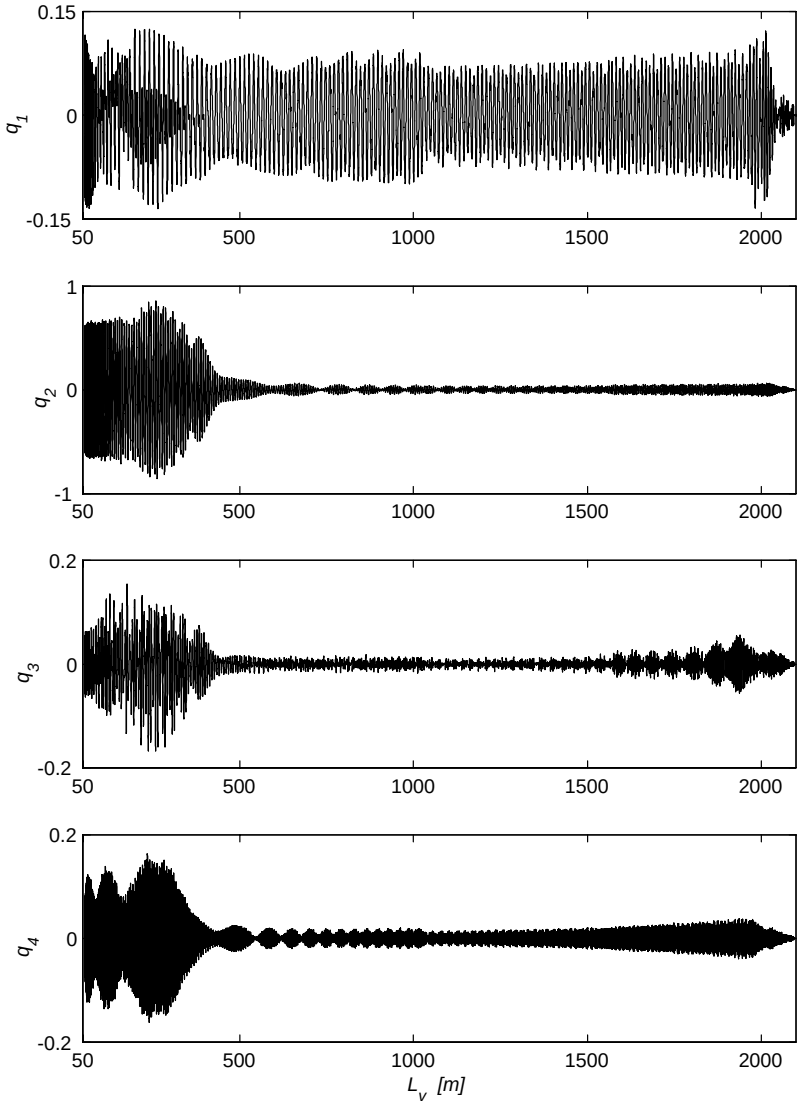

Fig. 22. Plots of the lateral out-of-plane modal co-ordinates, $V_c = 14\,\mathrm{m/s}$.

weight of the conveyance, represent the two actual catenaries and two vertical ropes. The simulation input parameters for this equivalent cable system are presented in Table 2, and the corresponding ascending winding cycle is considered.

The slow variation of the natural frequencies with the vertical rope length, and the resonance conditions arising in this system during the wind were analyzed in detail in Part 1. In this analysis, the first four longitudinal and lateral modes as well as the first and the second harmonics of the excitation were taken into account. It is evident that the system eigenvalues are widely spread, especially at the end of the wind, when the lateral modes are of low frequency and the third and the fourth longitudinal frequencies reach high values. Therefore, the complete solution to the

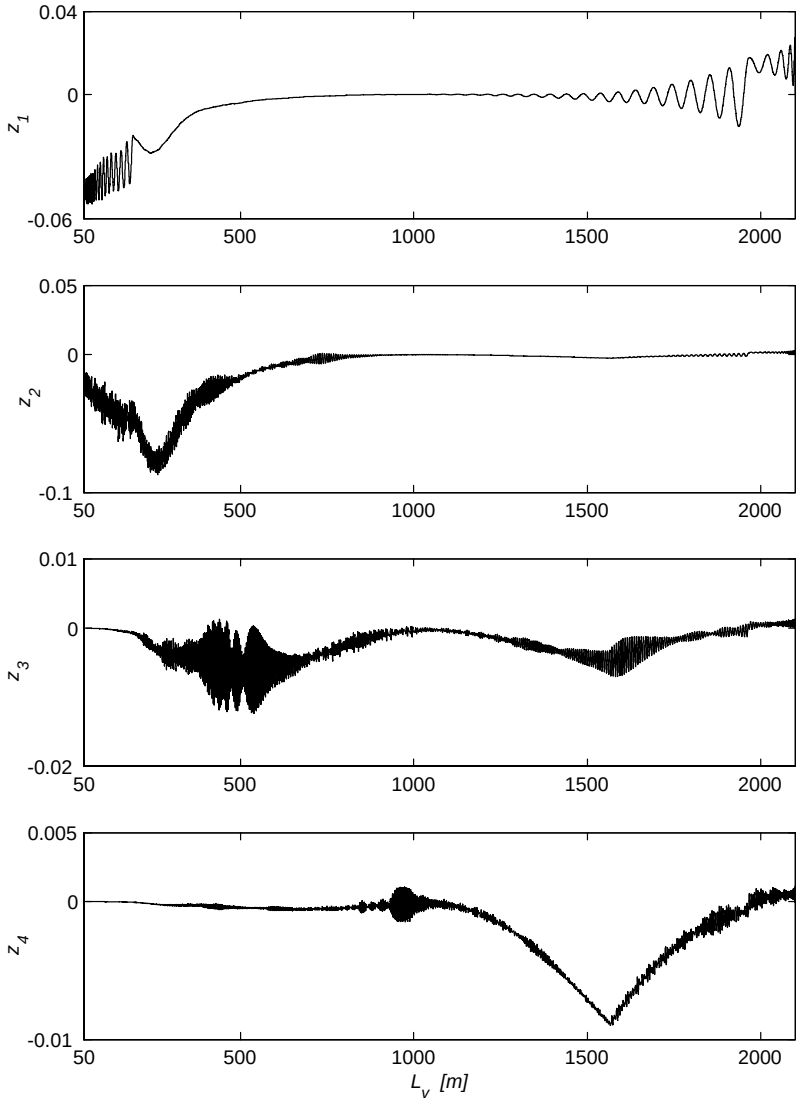

Fig. 23. Plots of the longitudinal modal co-ordinates, $V_c = 14\,\mathrm{m/s}$.

problem will consist of slow and fast components. Consequently, the dynamics of the deep mine winder system represents a *stiff* problem [16], and if the numerical solution is to return the entire transient response of the system over a long time interval, integration must be performed using relatively large time step to cover the slow components. However, the time step must be also small enough to capture the fast components, and to keep the numerical solution within acceptable bounds. Thus, due to these requirements integration methods not designed for stiff problems are ineffective, and lead to unstable results when applied to stiff equations.

The problem of numerical integration of systems of stiff ordinary differential equations has attracted considerable attention, and a number of efficient integration algorithms that

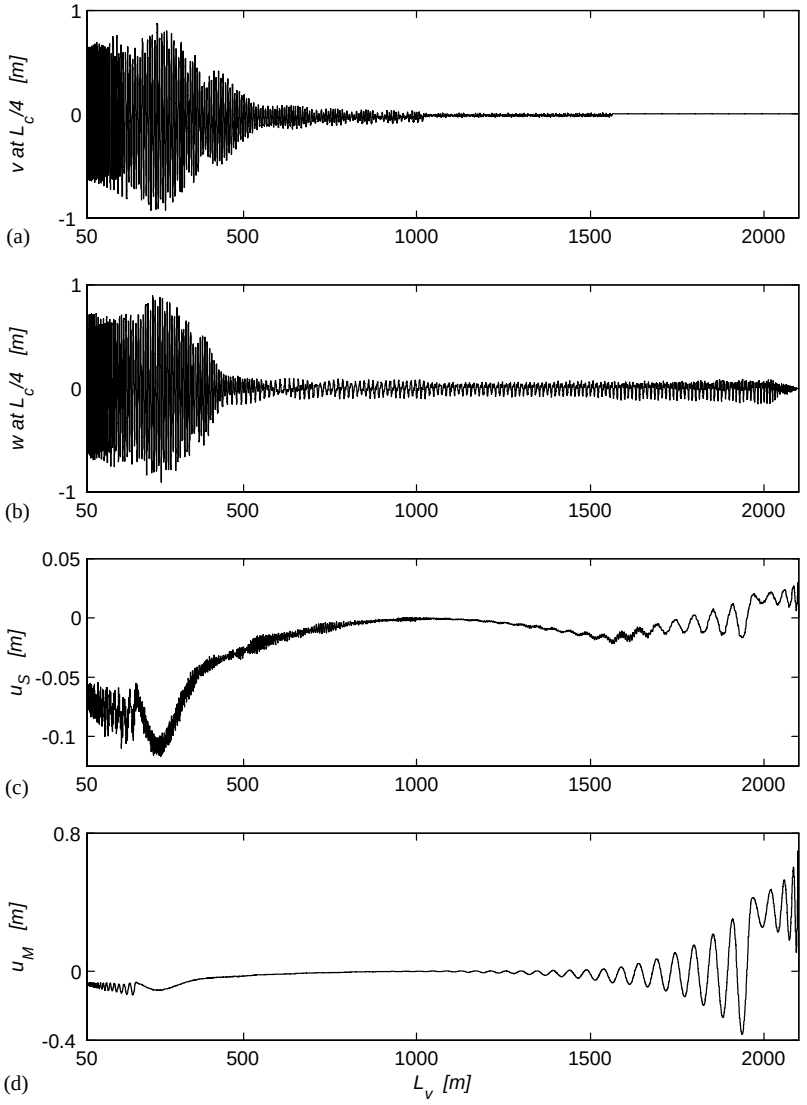

Fig. 24. Displacement response plots for $V_c = 14\,\mathrm{m/s}$: lateral (a) in-plane motions and (b) out-of-plane motions at the first quarter of the catenary longitudinal responses (c) at the sheave and (d) at the conveyance.

allow relatively large time steps, and that guarantee stability and bounded numerical error are available [17,18]. Multi-step methods based on backward differentiation formulas (BDFs, also known as Gear's method) have been the most prominent and most widely used for solving stiff problems. Recently, a new family of formulas called the numerical differentiation formulas (NDFs) have been developed and implemented in the MATLAB ODE suite [19]. They are more efficient than the BDFs, though the higher order formulas in this family are somewhat less stable. Both BDFs and NDFs codes are available from the ode15s MATLAB solver.

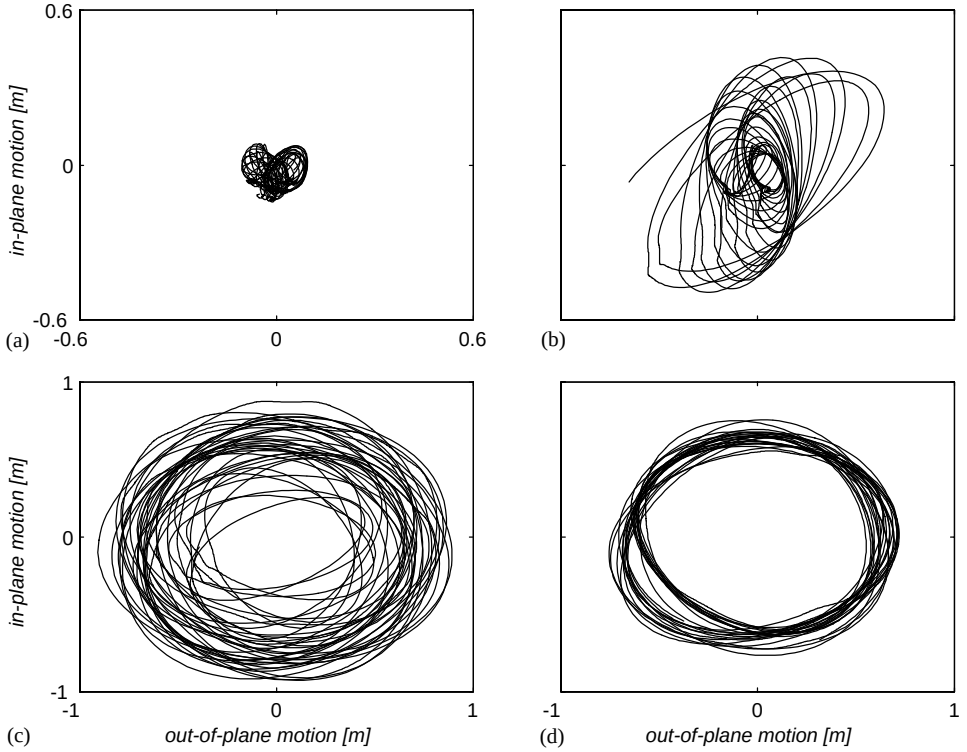

Fig. 25. The trajectory of the first quarter point of the catenary during various stages of the ascending cycle at $V_c = 14\,\mathrm{m/s}$: (a) $L_v = 800-600\,\mathrm{m}$, (b) $L_v = 600-400\,\mathrm{m}$, (c) $L_v = 400-150\,\mathrm{m}$, (d) $L_v = 150–60\,\mathrm{m}$.

The objective of the simulation is to predict the dynamic response due to the resonance and modal interaction phenomena discussed in Part 1. Thus, the cable longitudinal and lateral modes of order five and higher are neglected in the computations since they do not affect these phenomena. Consequently, Eq. (1) is coded in a MATLAB ODE file, and the ode15s stiff solver function is applied to the problem. The solver is invoked with the numerical differentiation formulas chosen to implement the integration. The relative accuracy tolerance $RelTol = 10^{-4}$ and the default absolute error tolerance $\mathrm{AbsTol} = 10^{-6}$ are used to monitor and to control the error at each integration step. In order to improve the efficiency of the calculations the total time span of the simulation is broken into a number of smaller steps.[2] The natural frequencies, the time-varying coefficients, and the excitation parameters are determined in advance and are made available in look-up tables as functions of slowly varying length $l(\tau)$. The actual values of these non-stationary characteristics are determined at each step of the integration by means of linear interpolation.

[2] The solver uses as many time points as necessary to produce a smooth solution. If the ODE function changes on a time scale that is very short compared to the simulation time span, then the solver will use a large number of time steps. This is the case in the present problem, as the simulation time span of the entire winding cycle is long (for the nominal velocity of $V_c = 15\,\mathrm{m/s}$ it exceeds 156 s).

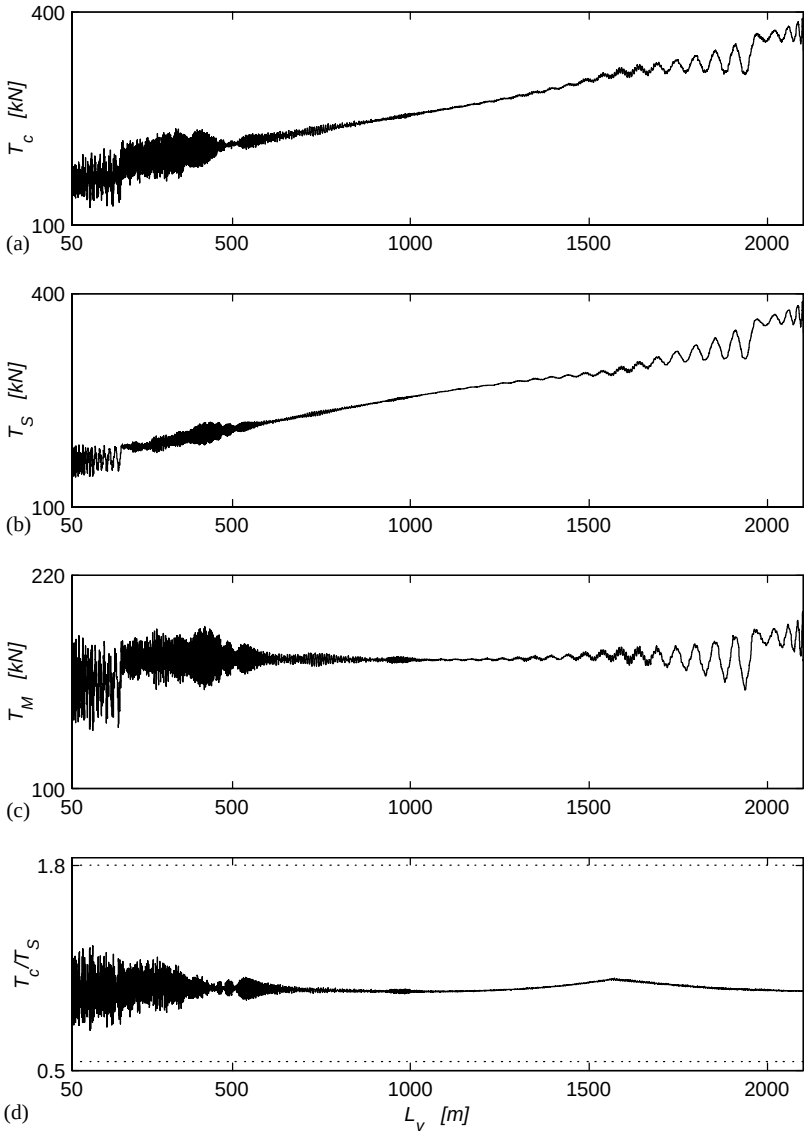

Fig. 26. Total tensions in the winding cables at the winding velocity $V_c = 14\,\mathrm{m/s}$. (a) the catenary tension T_c; (b) the vertical rope tension T_S at the sheave; (c) the vertical rope tension T_M at the conveyance; and (d) the tension ratio across the sheave T_c/T_S.

3.4. Nominal winding velocity

The simulation results for a cycle with the nominal winding velocity $V_c = 15\,\mathrm{m/s}$ are presented in what follows. The modal co-ordinates are plotted against the vertical rope length (shaft depth) L_v in Figs. 3–5. These are followed by the modal state-space plots and the response power spectra in Figs. 6–14, which represent three different time windows corresponding to the depth limits

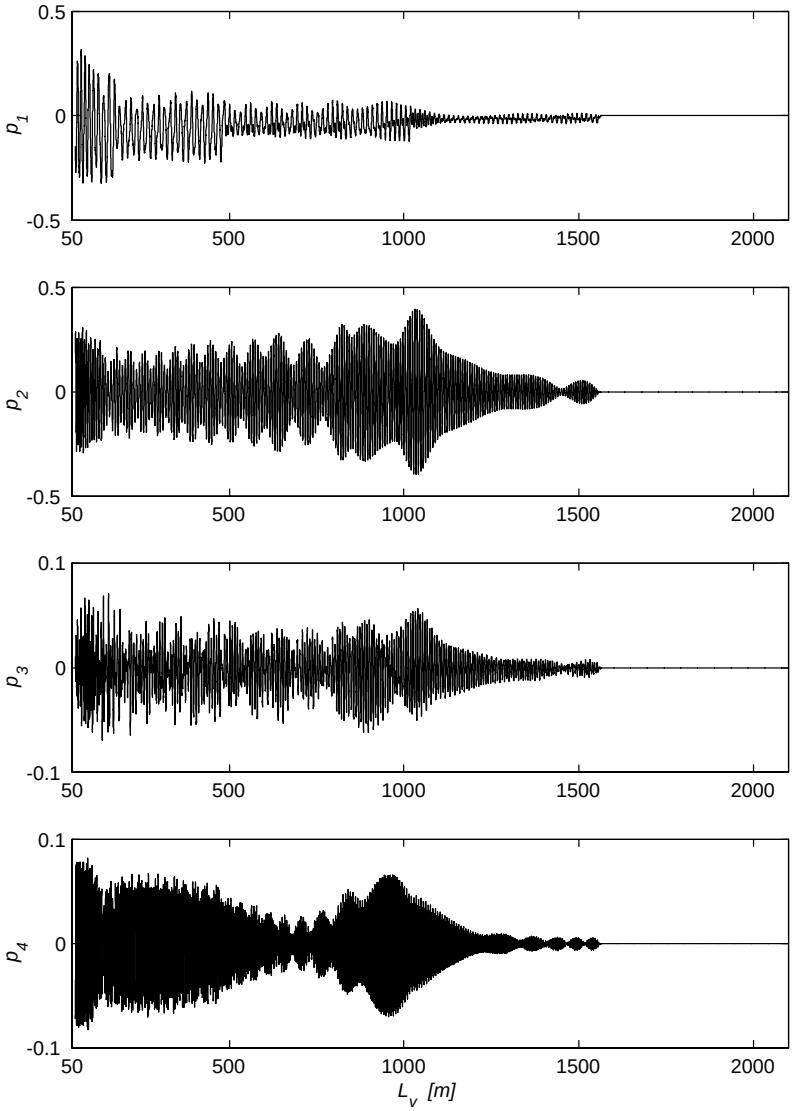

Fig. 27. Plots of the lateral in-plane modal co-ordinates, $V_c = 16\,\mathrm{m/s}$.

1000–800, 800–600 and 600–400 m, respectively. The displacement response plots are given in Fig. 15, where the lateral motions at the first quarter point of the catenary cable, and the longitudinal motions at the sheave and at the conveyance versus the vertical length are presented. The whirling motion of the catenary cable is further illustrated in Figs. 16–18. Namely, the lateral motion at the first quarter point of the catenary against the vertical length is presented in Fig. 16, and the trajectory of this point is illustrated in more detail in eight different time windows in Figs. 17 and 18. The total cable tension plots versus the vertical length, together with the tension ratio across the sheave plot, are shown in Fig. 19. This is followed by the dynamic cable tension plots given in Fig. 20.

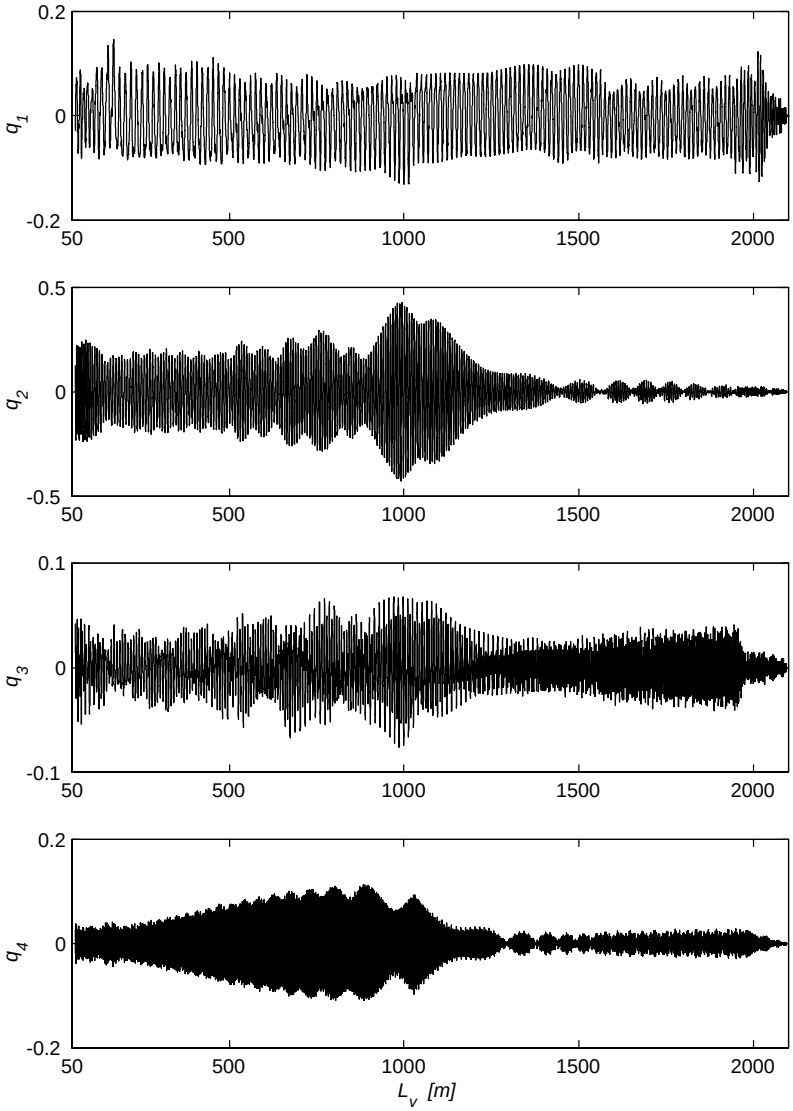

Fig. 28. Plots of the lateral out-of-plane modal co-ordinates, $V_c = 16\,\mathrm{m/s}$.

The simulation results demonstrate the dynamic phenomena occurring during the wind. When the conveyance accelerates from the bottom of the shaft, the acceleration inertial load results in a transient response, evident in the longitudinal modal co-ordinate plots (Fig. 5) and in the longitudinal displacement plots (Fig. 15c and d). A similar effect can be noted when the conveyance is decelerated to rest at the end of the wind. The effect of transition from the acceleration phase to the constant velocity phase, and from the constant velocity phase to the deceleration phase is clearly visible as a rapid change in the mean value of the longitudinal response. The catenary response is planar between the start of the wind and the first layer change,

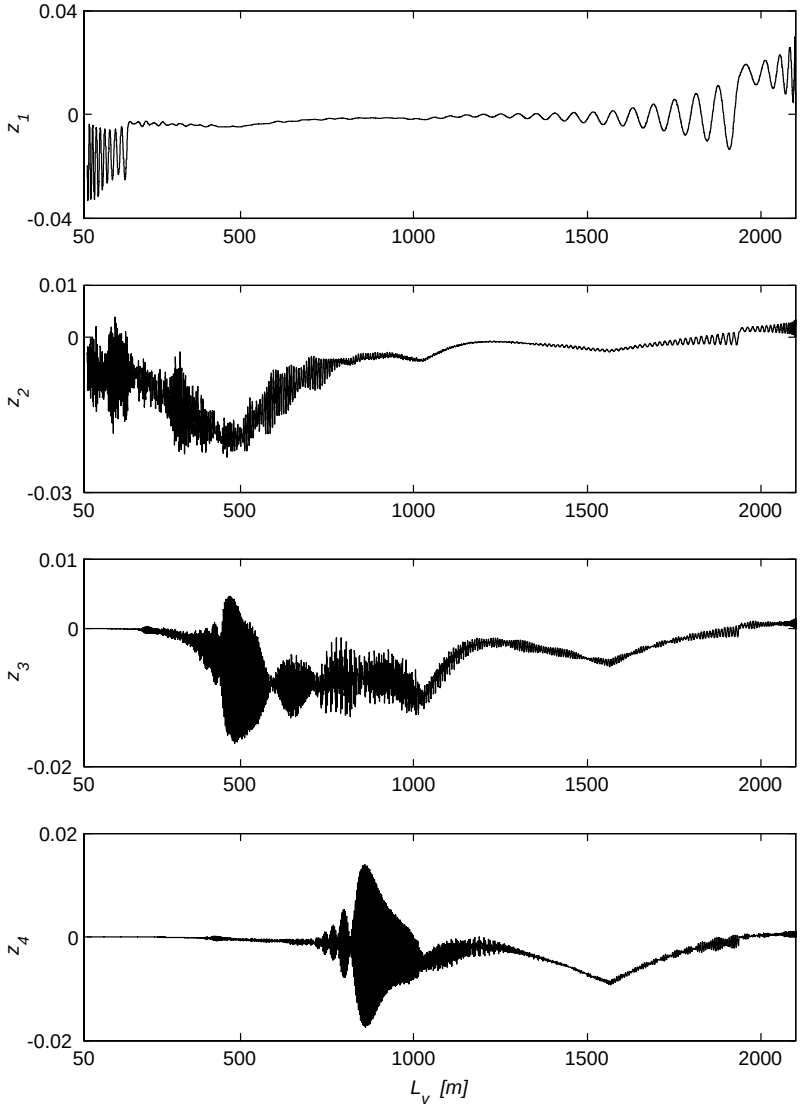

Fig. 29. Plots of the longitudinal modal co-ordinates, $V_c = 16\,\mathrm{m/s}$.

as evident in the in-plane lateral response (Fig. 3) and taking place at approximately $L_v = 1600\,\mathrm{m}$. The longitudinal co-ordinates and the corresponding displacements exhibit drifts in agreement with the overall lateral out-of-plane cable motion across the winding drum. This means that the longitudinal motions digress in the negative direction during the first layer, and go off in the opposite direction during the second layer. This pattern repeats itself throughout the wind.

The response plots versus the depth L_v along with phase (orbit) plots, and associated frequency power spectra shown in Figs. 6–14, illustrate the problematic dynamic behaviour of the system when a passage through the regions of instability occurs due to the resonance conditions described

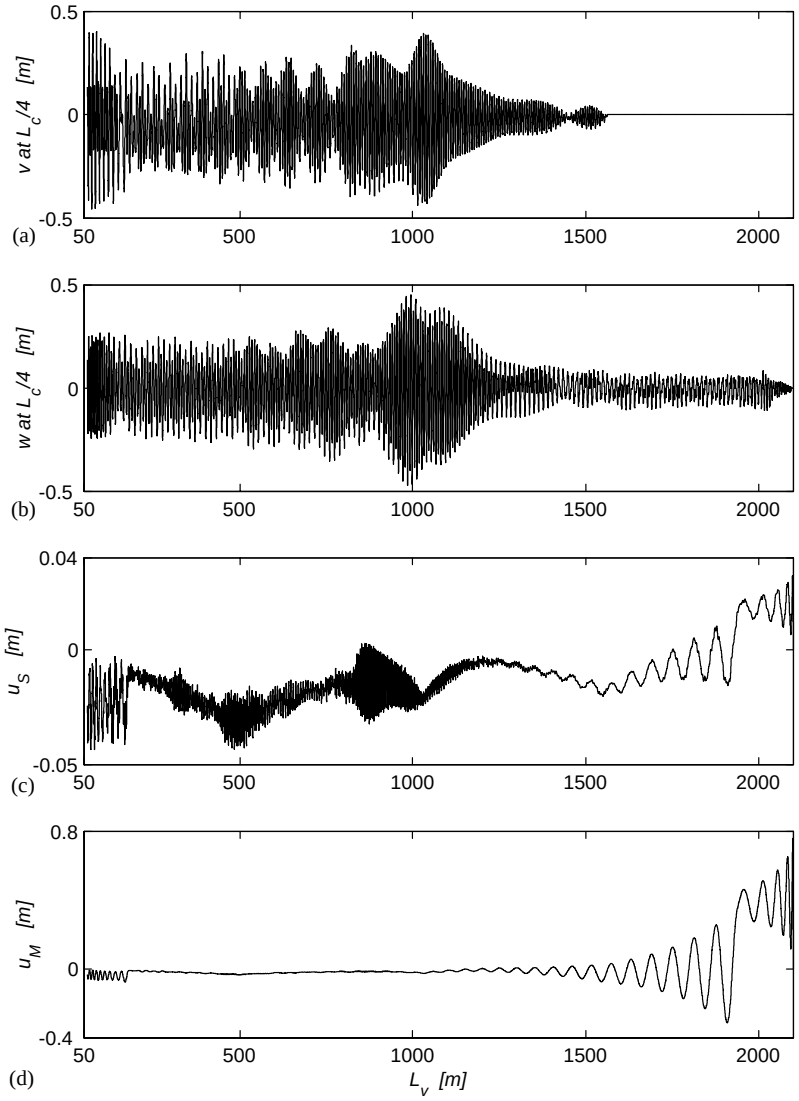

Fig. 30. Displacement response plots for $V_c = 16\,\mathrm{m/s}$: lateral (a) in-plane motions and (b) out-of-plane motions at the first quarter of the catenary; longitudinal responses (c) at the sheave and (d) at the conveyance.

in Part 1. The fundamental excitation frequency corresponding to the nominal winding speed of 15 m/s is 2.23 Hz, and peaks corresponding to this frequency as well as to its harmonics and subharmonics are evident in the system response. It should be noted that the associated phase portraits show crossings/twisting of the phase trajectories demonstrating the non-stationary/transient character of the motions.

Considering the depth region $L_v = 1000$–$800\,\mathrm{m}$, the primary resonance $\Omega_2 = \omega_4$ is apparent in the fourth longitudinal modal co-ordinate plot of Fig. 5, and in the power spectrum presented in Fig. 8. At the same time, a passage through the autoparametric resonance $\omega_4 \approx 2\bar{\omega}_2$ of the second

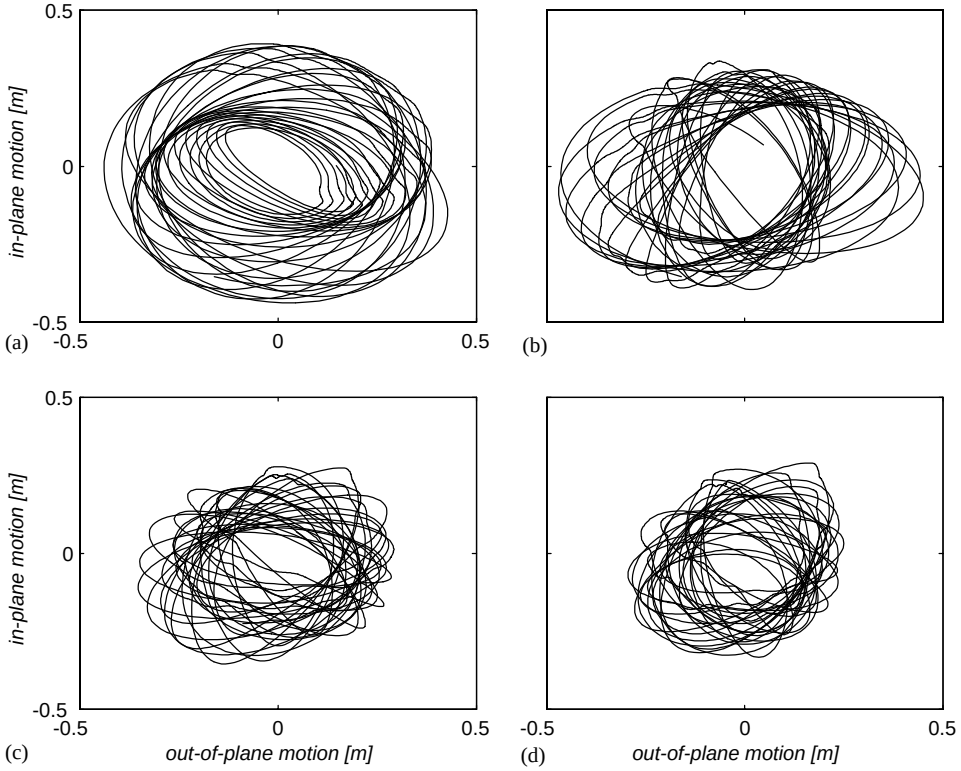

Fig. 31. The trajectory of the first quarter point of the catenary during various stages of the ascending cycle at $V_c = 16\,\mathrm{m/s}$: (a) $L_v = 1200-1000\,\mathrm{m}$, (b) $L_v = 1000-800\,\mathrm{m}$, (c) $L_v = 800-600\,\mathrm{m}$, (d) $L_v = 600–400\,\mathrm{m}$.

lateral mode shows in corresponding lateral co-ordinate response plots. In the depth region $L_v = 800-600\,\mathrm{m}$, large lateral motions and substantial longitudinal response occur. At this stage of the winding cycle, the system passes through the primary resonances $\Omega_1 \approx \omega_2 \approx \bar{\omega}_2$ and $\Omega_2 \approx \bar{\omega}_4$. It should be noted that the out-of-plane lateral motions are strongly excited, with the in-plane excitation being much smaller throughout the wind. It is interesting to observe that in this instability region, the second mode of the in-plane response continues to grow after the out-of-plane response has reached its peak value. Hence, it is evident that the large in-plane response is a direct consequence of the autoparametric 1:1 resonance and of the energy exchange between the lateral modes, with the out-of-plane motion being essentially a parametric excitation for the in-plane motion. The lateral response remains large beyond the 600 m depth level, due to cascading energy exchanges among the modes. This is evident from a visual inspection of response plots shown in Fig. 15, and also from the illustration of the tubular motion at the first quarter point of the catenary given in Fig. 16. The trajectory plots of lateral motion at this point presented in Figs. 17 and 18 show that up to the level $L_v \approx 1000\,\mathrm{m}$ the catenary response is small. Afterwards it grows, and in the region of approximately 800–600 m the cable begins to whirl, and consequently, a full ballooning motion develops in the region of 600–400 m, which persists till the end of the simulation.

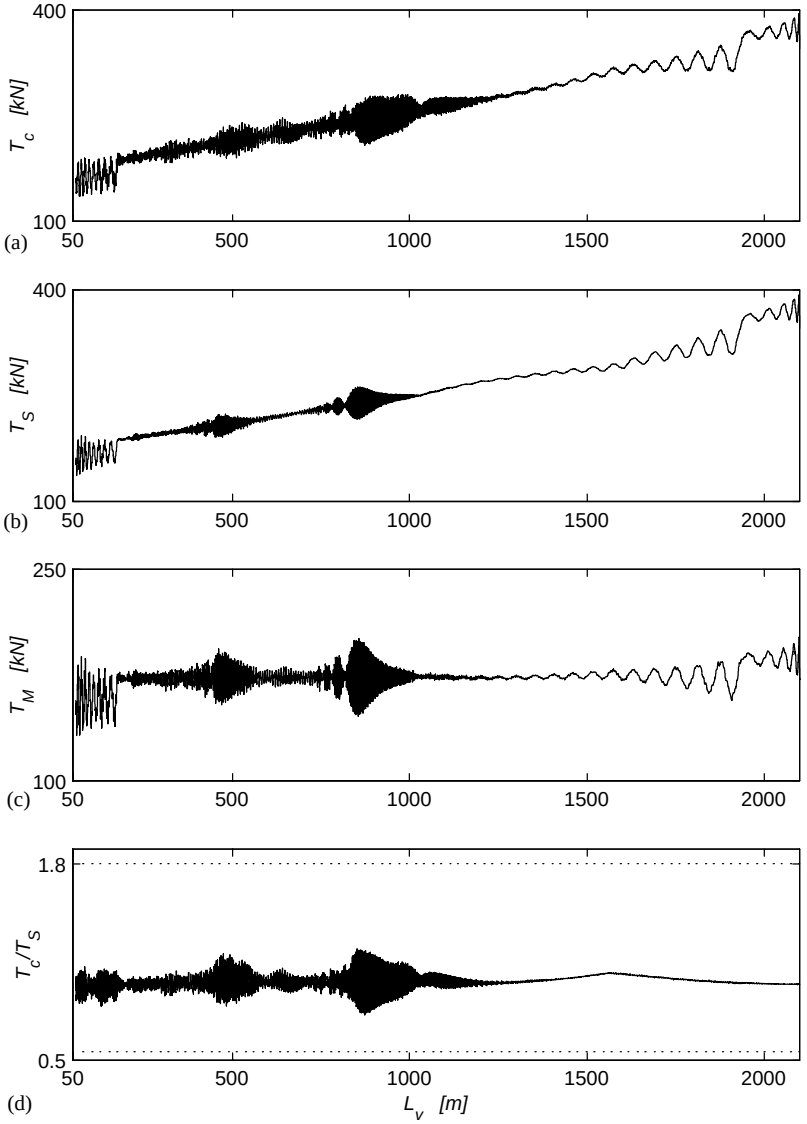

Fig. 32. Total tensions in the winding cables at the winding velocity $V_c = 16\,\mathrm{m/s}$: (a) the catenary tension T_c; (b) the vertical rope tension T_S at the sheave; (c) the vertical rope tension T_M at the conveyance; and (d) the tension ratio across the sheave T_c/T_S.

The dynamic behaviour of the system is further demonstrated in the cable tension plots. From an inspection of the total cable tension plots given in Fig. 19, it is evident that the mean catenary tension and the mean vertical rope tension at the sheave decrease during the up-wind due to the decreasing length of the vertical rope. Significant oscillations in the tensions occur at the beginning of the ascending cycle. These oscillations, caused by the initial acceleration inertial load, are of low frequency and become small after approximately 1500 m depth level. Large tension fluctuations begin to take place from the 1000 m level

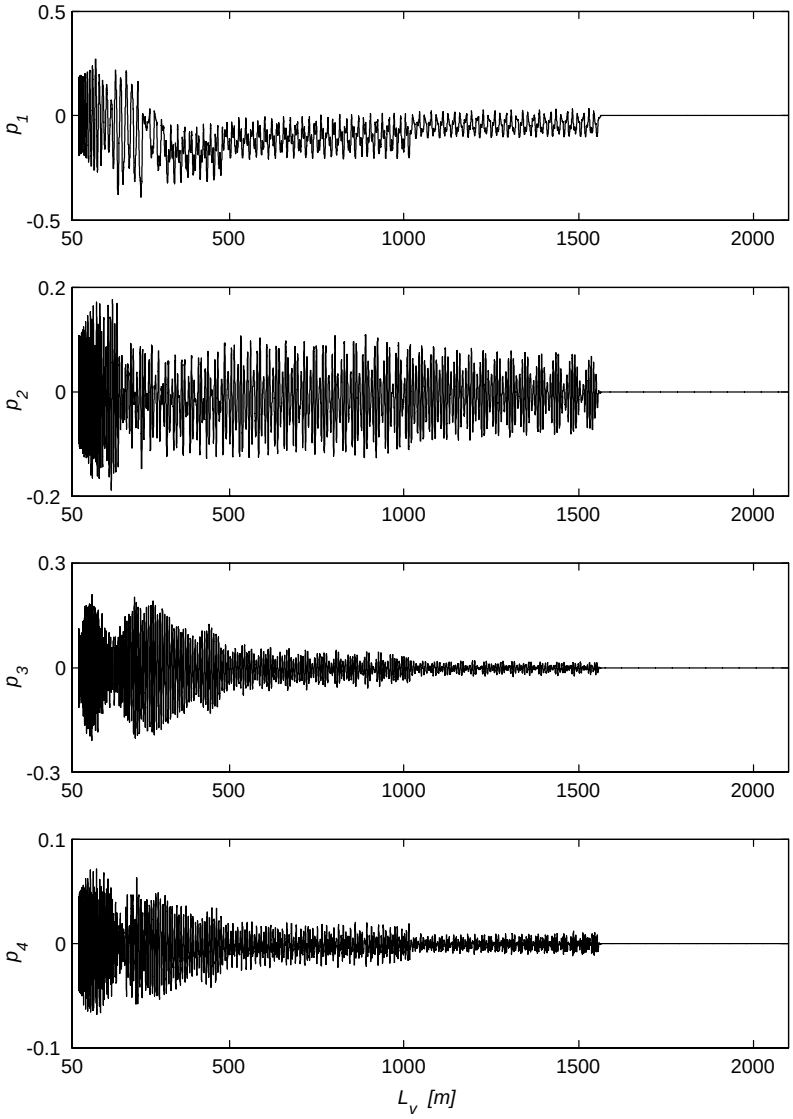

Fig. 33. Plots of the lateral in-plane modal co-ordinates, $V_c = 19.5\,\mathrm{m/s}$.

and continue till the end of the wind. They result from the non-linear modal interactions and resonance phenomena occurring in the system. It should be noted, however, that the tension ratio across the sheave does not exceed the limits for no slip.[3] The tension

[3] The equation governing the impending slipping of the rope around a pulley may be written in the classical form $T_2 = T_1 e^{-\mu\alpha}$, where T_1 and T_2 are the larger tensile force and the smaller tensile force, respectively, in the two parts of the rope not in contact with the pulley, μ is the coefficient of friction, and α denotes the angle of contact. This relationship can be used to formulate a criterion for no slip between the cable and the headsheave in the hoisting system, requiring that $e^{-\mu\alpha} < T_c/T_s < e^{\mu\alpha}$. Using the average value of $\mu = 0.25$, and the angle $\alpha = 135^\circ$, this criterion shows that the tension ratio must be within the limits [0.5559,1.8023] for slip not to occur.

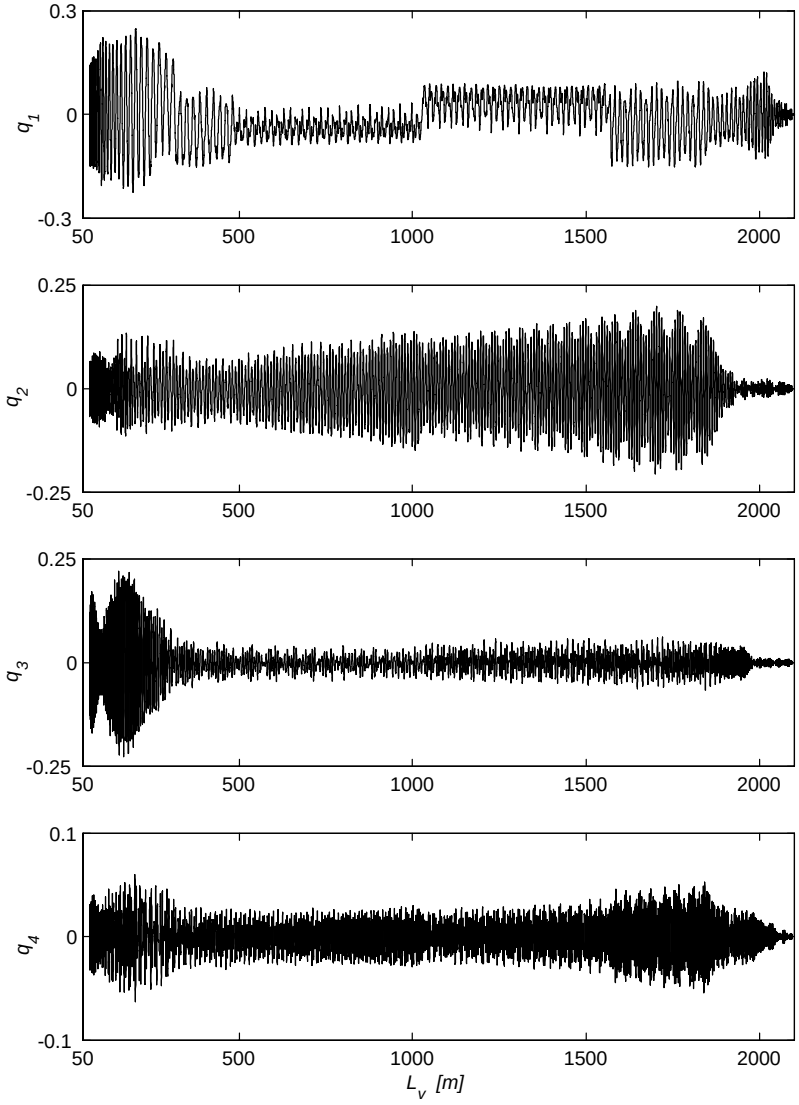

Fig. 34. Plots of the lateral out-of-plane modal co-ordinates, $V_c = 19.5\,\mathrm{m/s}$.

oscillations are better illustrated in Fig. 20. It can be seen that the most severe tension oscillations occur in the catenary, and are caused by large lateral motions of this cable.

3.5. Other winding velocity regimes

Changes in the winding velocity can shift the resonance locations, and the winding velocity is the most important parameter of the system. In order to investigate and to predict the system response under various winding velocity regimes simulations are carried out for other than the nominal velocity values. Namely, the response at the winding velocities $V_c = 14$, 16 and

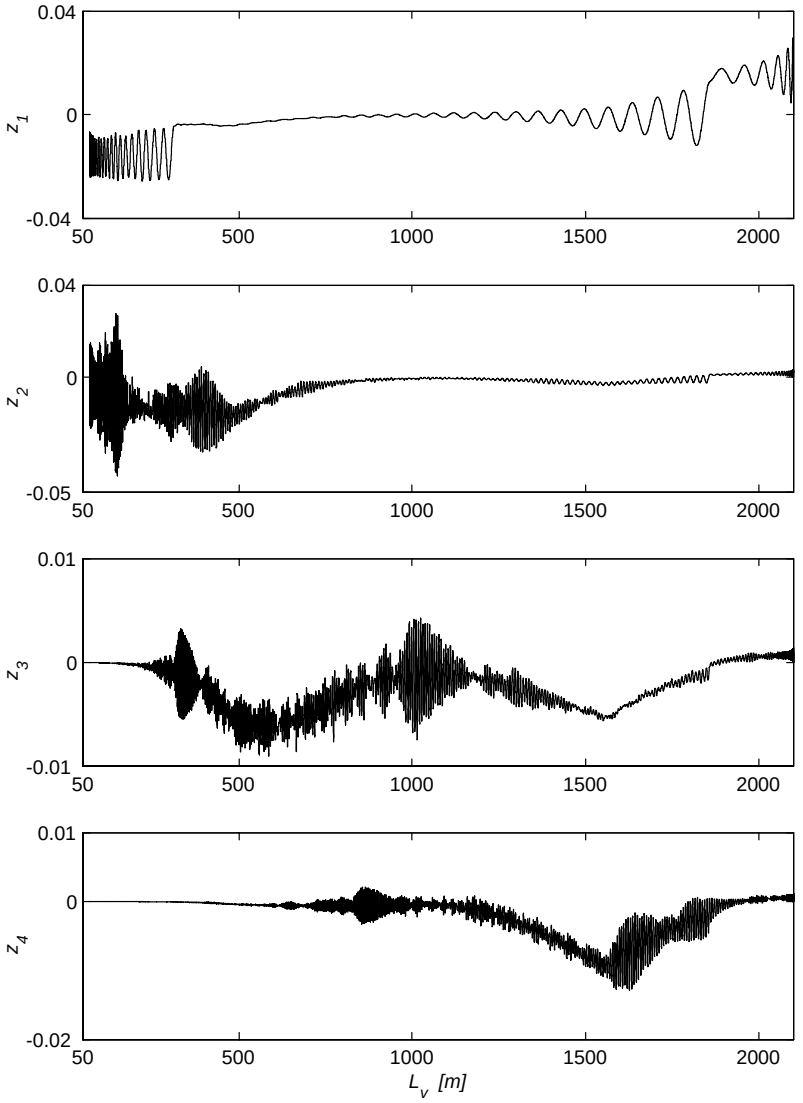

Fig. 35. Plots of the longitudinal modal co-ordinates, $V_c = 19.5\,\mathrm{m/s}$.

19.5 m/s are investigated. The resonance locations at these regimes have already been discussed in Part 1.

The simulation results for the winding velocity $V_c = 14\,\mathrm{m/s}$ are presented in Figs. 21–26. The modal co-ordinates are plotted against the vertical rope length L_v in Figs. 21–23, and the displacements in the system are presented in Fig. 24. As one can observe, the system develops a large dynamic response after a depth of approximately 500 m. As revealed in the frequency tuning analysis of Part 1, at a depth of $L_v = 400\,\mathrm{m}$, the primary resonances $\Omega_1 \approx \bar{\omega}_2$ and $\Omega_2 \approx \bar{\omega}_4$ occur, and the catenary cable is simultaneously involved in the principal parametric resonances $\Omega_1 \approx 2\bar{\omega}_1$ and $\Omega_2 \approx 2\bar{\omega}_2$. Autoparametric interactions between the in- and out-of-plane lateral modes also

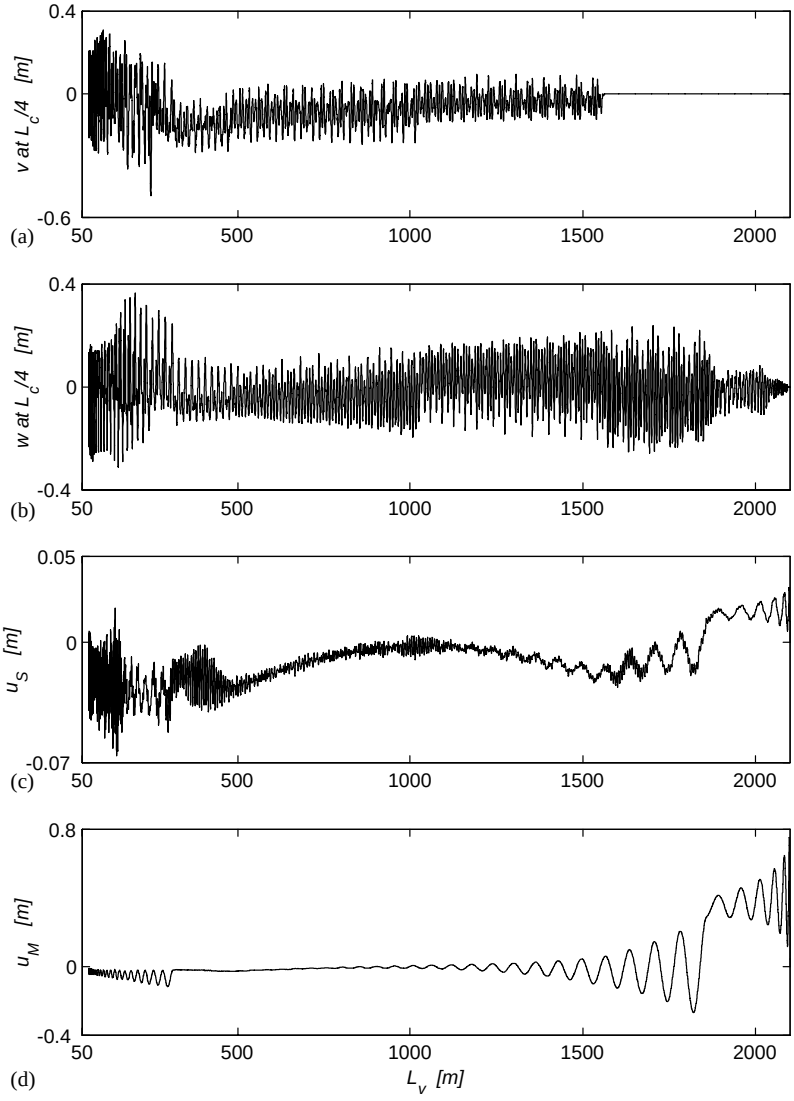

Fig. 36. Displacement response plots for $V_c = 19.5\,\mathrm{m/s}$: lateral (a) in-plane motions and (b) out-of-plane motions at the first quarter of the catenary; longitudinal responses (c) at the sheave and (d) at the conveyance.

occur, and these resonance conditions produce large catenary ballooning motions. As one can see from plots given in Figs. 24 and 25, the amplitudes of these motions approach 1 m. This large lateral catenary response affects the longitudinal response significantly. This effect can be observed in the first, second and in the third modal longitudinal co-ordinate plots presented in Fig. 23, and in the displacement response at the sheave and at the conveyance shown in Fig. 24. Besides, passages through longitudinal primary resonances occur at various shaft depth levels. Namely, the resonance conditions $\Omega_1 \approx \omega_3$ at $L_v \approx 1700\,\mathrm{m}$, $\Omega_2 \approx \omega_4$ at $L_v \approx 1000\,\mathrm{m}$, $\Omega_1 \approx \omega_2$ at

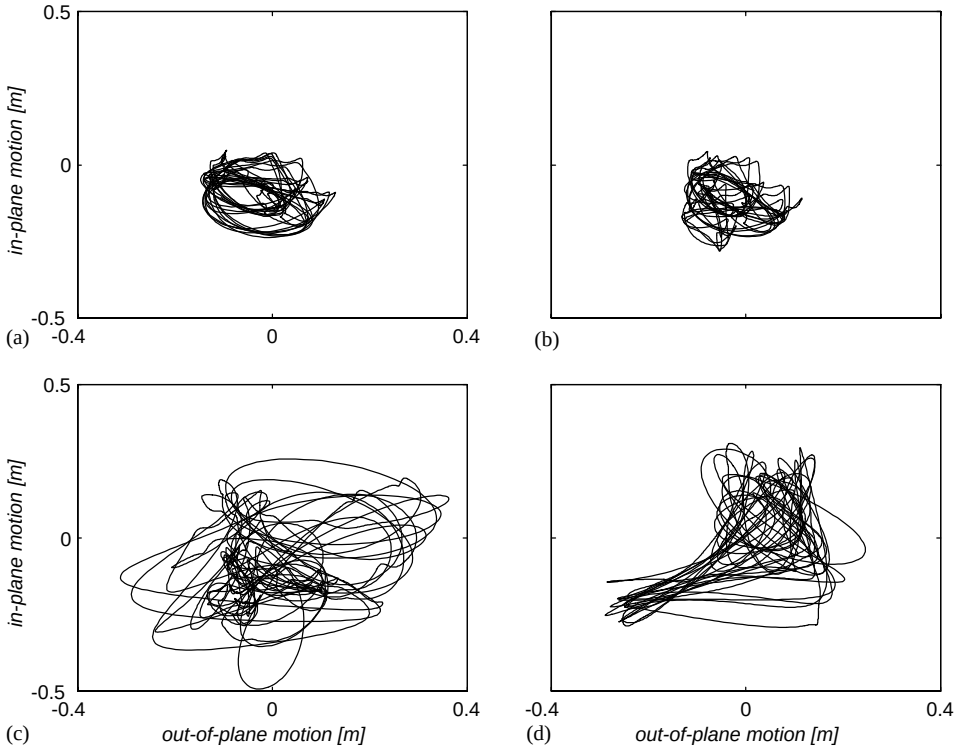

Fig. 37. The trajectory of the first quarter point of the catenary during various stages of the ascending cycle at $V_c = 19.5\,\mathrm{m/s}$: (a) $L_v = 800$–$600\,\mathrm{m}$, (b) $L_v = 600$–$400\,\mathrm{m}$, (c) $L_v = 400$–$150\,\mathrm{m}$, (d) $L_v = 150$–$70\,\mathrm{m}$.

$L_v \approx 800\,\mathrm{m}$ and $\Omega_2 \approx \omega_3$ at $L_v \approx 550\,\mathrm{m}$ are reflected in the modal co-ordinate plots. To conclude this set of results, the total cable tension plots are presented in Fig. 26. As expected, significant oscillations in the cable tensions arise in the catenary resonance region. However, the limits for no slip are not exceeded.

Furthermore, the simulation results for the winding velocity $V_c = 16\,\mathrm{m/s}$ are presented in Figs. 27–32, where the modal co-ordinates are plotted against time, the cable displacements are shown versus the shaft depth, the trajectory of the first quarter point of the catenary cable is illustrated in four time windows, and the total tensions plots are shown. In this case, the primary and parametric catenary resonances occur at the depth $L_v \approx 1150\,\mathrm{m}$ which is clearly visible in these figures. As in the previous simulations, amplitude-modulated whirling catenary cable motions result, which promote a significant longitudinal response at the sheave presented. The system also passes through a number of primary longitudinal resonances, which are noticeable in the tension plots. However, as in the previous cases, the tension ratio across the sheave remains within the no slip range.

In order to avoid the catenary resonances the winding velocity can be increased up to 19.5 m/s, as indicated in the resonance analysis of Part 1. The simulation results for this case are shown in Figs. 33–38. It is noticeable that the system response remains small for the most part of the wind, with an increase taking place only at the end of the cycle. This increase can be attributed to the

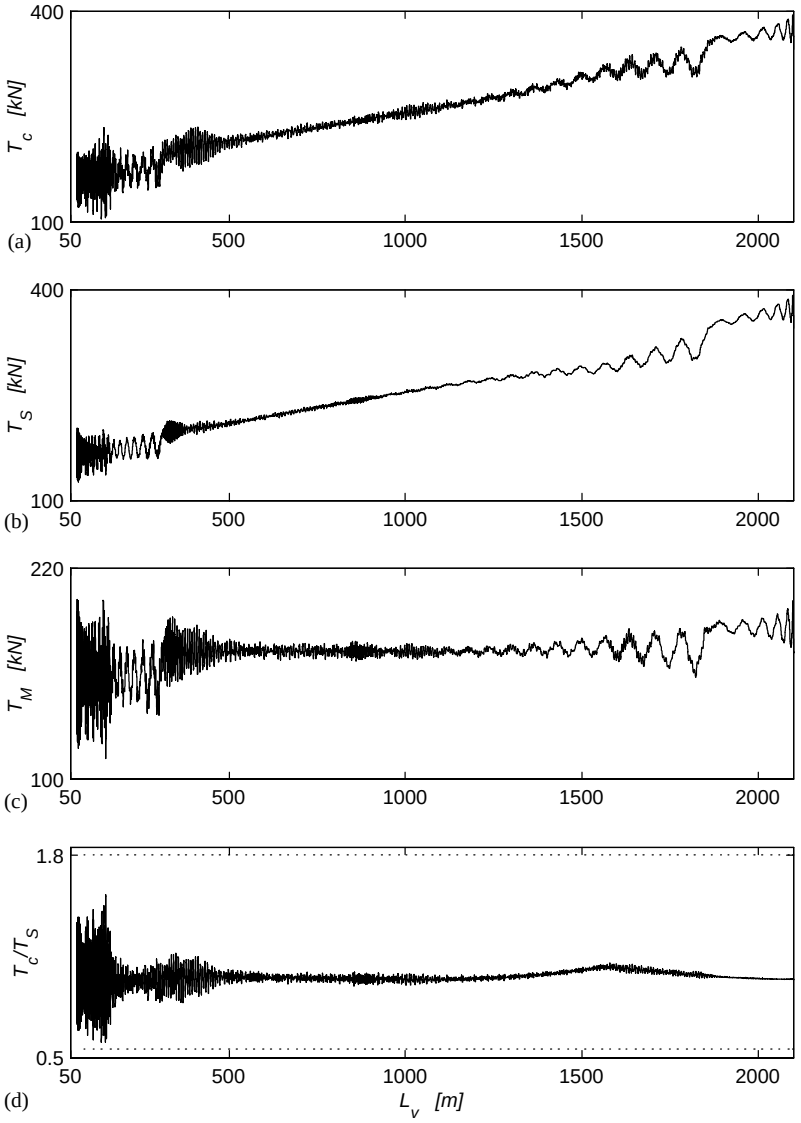

Fig. 38. Total tensions in the winding cables at the winding velocity $V_c = 19.5\,\mathrm{m/s}$: (a) the catenary tension T_c; (b) the vertical rope tension T_S at the sheave; (c) the vertical rope tension T_M at the conveyance; and (d) the tension ratio across the sheave T_c/T_S.

fact that at the end of the wind, the fundamental harmonic of the excitation becomes close to the third lateral natural frequency, namely $\Omega_1 \approx \bar{\omega}_3$. Also, several longitudinal resonances occur during the wind and are manifested in the longitudinal modal co-ordinate plots. Since it is not possible to suppress the longitudinal resonances within the winding cycle through the winding velocity change, the corresponding cable tension fluctuations occur, as can be seen in Fig. 38.

4. Conclusions

The results of numerical simulations of ascending cycles using the non-linear model of a hoisting cable system, based on the parameters of a typical double-drum BMR winding plant, show a vast range of interesting and potentially dangerous non-linear dynamic phenomena.

The nominal cycle simulation with winding velocity $V_c = 15\,\mathrm{m/s}$ demonstrates problematic dynamic behaviour from the depth level of approximately 900 m. It should be noted that the results of this simulation corroborate the observations recorded during the operation of Kloof Gold Mine rock winder, a BMR system with its nominal parameters corresponding to the parameters used in the simulation [15]. It was recorded that from the depth of 900 m during ascending cycles the catenary amplitudes increased with the second mode (full sine-wave) clearly identified, both in the in-plane and out-of-plane motion of the catenaries. The amplitude of the out-of-plane vibration was usually larger and was judged to be of the order of 1 m. This correlates well with the whirling-motion amplitude obtained from the simulation. The adverse dynamic behaviour of the system is caused largely by the primary catenary even (second and fourth) resonances, and by the autoparametric interactions between the in- and out-of-plane catenary modes. Principal parametric resonances of the lateral modes also occur, and conditions for autoparametric interactions between the lateral and longitudinal modes arise. Additionally, a transition through a number of primary longitudinal resonances takes place during the wind. It should also be noted that the adverse dynamic motions in the system promote large oscillations in the cable tension. These oscillations must be considered significant with respect to fatigue of the cable, and may lead to strand failures in wire ropes. Such failures occurred recently in deep mine sinking operations carried out by the South African mining industry, and resulted in winding ropes being discarded after an unacceptably low number of working cycles [20].

When the winding velocity is changed the resonance locations are shifted. The simulation of the winding cycle at 14 m/s demonstrates that the primary catenary resonances are moved towards the end of the wind, and thus the catenary response is decreased throughout the main part of the cycle. The strategy of decreased winding velocity had often been applied in practice in Kloof winding installation, as reported in the observations documented by Dimitriou and Whillier [15]. However, the simulation predicts large catenary whirling motions at the end of the wind at this winding velocity. The simulation results for 16 m/s further clarifies the role of the location of the primary catenary resonances, and confirm the autoparametric nature of the system. Hence, it is evident that the catenary resonances can be avoided, to a large extent, if the winding velocity is increased to an appropriate level. For example, for the installation considered in this investigation, a velocity of about 19.5 m/s could be applied on the ascending cycle in order to achieve suitable resonance shifts. The simulation results for this velocity confirm the benefits of this strategy.

The simulation results illustrate the complexity of the dynamic behaviour of deep mine hoisting cables during a winding cycle. A small change in the winding velocity may cause large changes in the dynamic response due to the resonance region shifts. The non-linear nature of the system is responsible for modal interactions and large amplitude catenary cable motions. The parameters of the system vary slowly and the motions exhibit non-stationary character. Consequently, the

response is qualitatively different from the response which would occur if the parameters were stationary.

It should be pointed out that the simulation results are based on a four-mode longitudinal and lateral approximation of the cable. Namely, the first four longitudinal and lateral modes that are dominant in the regions of adverse dynamic behaviour of the cable are considered in the simulation model. Consequently, this approximation can be considered as adequate to represent the response due to the passage through the resonance and modal interaction regions as discussed in this research.

An important issue in the response analysis of non-linear systems is the study of equilibrium solutions. It is known that as parameters in a non-linear system are changed the stability of the stationary equilibrium points can change as well as the number of equilibrium points. This qualitative change in the dynamic features of a system is referred to as bifurcation. Since parameters in the catenary–vertical rope system vary slowly during a winding cycle, a bifurcation to an alternative dynamic state can take place during the wind. It should be noted, however, that an effective bifurcation will occur away from the point at which the stationary (quasistatic) bifurcation takes place. Thus, the resulting motion might exhibit phenomena like sudden jumps and oscillations around the quasistatic equilibrium solutions [21]. This would have to be investigated in more detail in the subsequent studies in order to ensure the dynamic integrity of deep mine hoisting installations, especially in plants where shaft depths exceed 3000 m.

Appendix A. Nomenclature

A cable effective cross-sectional area
c longitudinal wave speed
$\bar{c}$ lateral wave speed
I mass moment of inertia of the sheave
M conveyance mass
m linear cable mass
l slowly varying length parameter
L_c catenary length
L_v vertical rope length
N_{lat} number of lateral modes
N_{long} number of longitudinal modes
p_n nth lateral in-plane modal co-ordinate
P_k lateral in-plane load
q_n nth lateral out-of-plane modal co-ordinate
Q_k lateral out-of-plane load
R sheave radius
s Lagrangian co-ordinate
t time
T fast time scale
T_c^i catenary mean tension

T_v^i vertical rope mean tension
u_v longitudinal displacement of the vertical rope
u_l longitudinal boundary excitation
v catenary in-plane lateral displacement
v_l lateral in-plane boundary excitation
w catenary out-of-plane lateral displacement
w_l lateral out-of-plane boundary excitation
z_n nth longitudinal modal co-ordinate
Z_r longitudinal load
Y_n nth longitudinal mode shape
γ_n longitudinal eigenvalue
ε small parameter
λ_i lateral damping coefficient
μ_i longitudinal damping coefficient
ω_n nth longitudinal natural frequency
$\bar{\omega}_n$ nth lateral natural frequency
Ω_n nth harmonic of excitation
$\bar{\varsigma}_n$ lateral damping ratio of the nth mode
τ slow time scale

References

[1] R.G. Gürtunca, South African mining industry in the new millennium and future challenges, Proceedings of the International Conference on Applied Mechanics SACAM, 2000, Durban, South Africa, 2000, pp. 24–35.
[2] S. Kaczmarczyk, Non-stationary Responses of Hoisting Cables with Slowly Varying Length, Ph.D. Thesis, School of Mechanical Engineering, University of Natal, Durban, South Africa, 1998.
[3] S. Kaczmarczyk, W. Ostachowicz, Transient vibration phenomena in deep mine hoisting cables. Part 1: Mathematical model, Journal of Sound and Vibration 262 (2003) 219–244, this issue.
[4] O.A. Goroshko, G.N. Savin, Introduction to Mechanics of One-Dimensional Bodies with Variable Length, Naukova Dumka, Kiev, 1971 (in Russian).
[5] R.R. Mankowski, F.J. Cox, Response of mine hoisting cables to longitudinal shock loads, Journal of the South African Institute of Mining and Metallurgy 86 (1986) 51–60.
[6] H.H. Vanderveldt, J.J. Gilheany, Propagation of a longitudinal pulse in wire ropes under axial loads, Experimental Mechanics 10 (1970) 401–407.
[7] C.P. Constancon, The Dynamics of Mine Hoist Catenaries, Ph.D. Thesis, Faculty of Engineering, University of the Witwatersrand, Johannesburg, South Africa, 1993.
[8] S. Kaczmarczyk, The passage through resonance in a catenary–vertical cable hoisting system with slowly varying length, Journal of Sound and Vibration 208 (1997) 243–269.
[9] A. Yu, Vibration damping of stranded cable, SESA Proceedings 9 (1952) 141–157.
[10] H.H. Vanderveldt, B.S. Chung, W.T. Reader, Some dynamic properties of axially loaded wire ropes, Experimental Mechanics 13 (1973) 24–30.
[11] H.M. Irvine, Cable Structures, The MIT Press, Cambridge, MA, 1981.
[12] R.R. Mankowski, Internal damping characteristics of a mine hoist cable undergoing non-planar transverse vibration, Journal of the South African Institute of Mining and Metallurgy 88 (1988) 401–410.
[13] R.R. Mankowski, Internal power losses occurring at the wavefront of travelling transverse disturbances on mine hoisting cables, Journal of the South African Institute of Mining and Metallurgy 90 (1990) 339–344.

[14] R.R. Mankowski, A Study of Nonlinear Vibrations Occurring in Mine Hoisting Cables, Ph.D. Thesis, Faculty of Engineering, University of the Witwatersrand, Johannesburg, South Africa, 1982.
[15] C. Dimitriou, A. Whillier, Vibrations in winding ropes: an appraisal, SAIMechE Hoisting Conference, Johannesburg, 1973.
[16] P.E. Nikravesh, Computer-Aided Analysis of Mechanical Systems, Prentice-Hall, Englewood Cliffs, NJ, 1988.
[17] E. Hairer, G. Wanner, Solving Ordinary Differential Equations II, Stiff and Differential—Algebraic Problems, Springer, Berlin, 1991.
[18] L.F. Shampine, Numerical Solution of Ordinary Differential Equations, Chapman & Hall, New York, 1994.
[19] L.F. Shampine, M. Reichelt, MATLAB Version 5 Help Documentation, The Matlab ODE suite, 1996.
[20] T.E. Wakefield, I.J. Wallace, P.J. Davidtsz, Rope experience gained from sinking the South Deep main and ventilation shafts, Mine Hoisting 2000 Fifth International Conference, Johannesburg, South Africa, The South African Institute of Mining and Metallurgy, Symposium Series S25, 2000.
[21] A. Raman, A.K. Bajaj, P. Davies, On the slow transition across instabilities in nonlinear dissipative systems, Journal of Sound and Vibration 192 (1996) 835–865.